Astronomy & Astrophysics

Investigating the young solar system analog HD 95086[*]

A combined HARPS and SPHERE exploration

G. Chauvin[1,2], R. Gratton[3], M. Bonnefoy[1], A.-M. Lagrange[1], J. de Boer[4], A. Vigan[5], H. Beust[1], C. Lazzoni[3],
A. Boccaletti[6], R. Galicher[6], S. Desidera[3], P. Delorme[1], M. Keppler[7], J. Lannier[1], A.-L. Maire[7], D. Mesa[3,20],
N. Meunier[1], Q. Kral[6], T. Henning[7], F. Menard[1], A. Moor[8], H. Avenhaus[9], A. Bazzon[9], M. Janson[7,10], J.-L. Beuzit[1],
T. Bhowmik[6], M. Bonavita[11], S. Borgniet[6], W. Brandner[7], A. Cheetham[12], M. Cudel[1], M. Feldt[7], C. Fontanive[11],
C. Ginski[13], J. Hagelberg[1], P. Janin-Potiron[14], E. Lagadec[14], M. Langlois[5,15], H. Le Coroller[5], S. Messina[16],
M. Meyer[8], D. Mouillet[1], S. Peretti[12], C. Perrot[6], L. Rodet[1], M. Samland[7], E. Sissa[3], J. Olofsson[7,17], G. Salter[5],
T. Schmidt[5], A. Zurlo[5,18,19], J. Milli[19], R. van Boekel[7], S. Quanz[8], P. Feautrier[1], D. Le Mignant[5], D. Perret[6],
J. Ramos[7], and S. Rochat[1]

(Affiliations can be found after the references)

ABSTRACT

Context. HD 95086 (A8V, 17 Myr) hosts a rare planetary system for which a multi-belt debris disk and a giant planet of 4–5 $M_{\rm Jup}$ have been directly imaged.
Aims. Our study aims to characterize the global architecture of this young system using the combination of radial velocity and direct imaging observations. We want to characterize the physical and orbital properties of HD 95086 b, search for additional planets at short and wide orbits and image the cold outer debris belt in scattered light.
Methods. We used HARPS at the ESO 3.6 m telescope to monitor the radial velocity of HD 95086 over two years and investigate the existence of giant planets at less than 3 au orbital distance. With the IRDIS dual-band imager and the IFS integral field spectrograph of SPHERE at VLT, we imaged the faint circumstellar environment beyond 10 au at six epochs between 2015 and 2017.
Results. We do not detect additional giant planets around HD 95086. We identify the nature (bound companion or background contaminant) of all point-like sources detected in the IRDIS field of view. None of them correspond to the ones recently discovered near the edge of the cold outer belt by ALMA. HD 95086 b is resolved for the first time in *J*-band with IFS. Its near-infrared spectral energy distribution is well fitted by a few dusty and/or young L7–L9 dwarf spectral templates. The extremely red 1–4 μm spectral distribution is typical of low-gravity objects at the L/T spectral type transition. The planet's orbital motion is resolved between January 2015 and May 2017. Together with past NaCo measurements properly re-calibrated, our orbital fitting solutions favor a retrograde low to moderate-eccentricity orbit $e = 0.2^{+0.3}_{-0.2}$, with a semi-major axis ~52 au corresponding to orbital periods of ~288 yr and an inclination that peaks at $i = 141°$, which is compatible with a planet-disk coplanar configuration. Finally, we report the detection in polarimetric differential imaging of the cold outer debris belt between 100 and 300 au, consistent in radial extent with recent ALMA 1.3 mm resolved observations.

Key words. instrumentation: adaptive optics – instrumentation: high angular resolution – methods: observational – stars: individual: HD 95086 – planet-disk interactions

1. Introduction

Dusty debris disks around pre- and main-sequence stars are signposts for the existence of planetesimals and exoplanets (Chen et al. 2012; Marshall et al. 2014). Numerous T Tauri and Herbig stars indicate that the characteristic timescale for the dispersal of their primordial dusty, gaseous disks is a few million years (Haisch et al. 2001, 2005; Fedele et al. 2010). Giant planet formation is expected to play a key role in the evolution from protoplanetary to debris disks. This is indirectly confirmed by submillimeter and near-infrared images of cool dusty debris disks around main sequence stars (Schneider et al. 2014b). The

presence of dust and the discovered disk structures (ring, gap, warp, and other asymmetries) could be indirect indicators of the presence of giant planets. In that context, it is striking to note that the majority of giant planets recently discovered in imaging have been found around young, dusty, early-type stars. This includes the breakthrough discoveries of HR 8799 bcde (5–10 $M_{\rm Jup}$ at 10–64 au, A8V star; Marois et al. 2008, 2010), β Pictoris b (8–13 $M_{\rm Jup}$ at 9 au, A5V star; Lagrange et al. 2010), HD 95086 b (4–5 $M_{\rm Jup}$ at 56 au, A8V star; Rameau et al. 2013b), and 51 Eri b (2 $M_{\rm Jup}$ at 14 au, F0V star; Macintosh et al. 2015) with the exception of HIP 65426 b (6–12 $M_{\rm Jup}$ at 92 au, A2V star; Chauvin et al. 2017a) which has no clear sign of debris disk in the system yet.

The source HD 95086 belongs to this group of young planetary systems for which a multi-belt debris disk and a giant planet have been directly imaged. The central star is an early-type A8V kinematic member of the Lower Centaurus Crux (LCC) association (Madsen et al. 2002; Rizzuto et al. 2012), located at

Table 1. Physical properties of HD 95086 from Moór et al. (2013) for $T_{\rm eff}$, log(g), [Fe/H], $v \sin(i)$, Pecaut et al. (2012) for age, Gaia Collaboration (2016) for distance, Siess et al. (2000) for predicted mass and luminosity, Cutri et al. (2003) and Høg et al. (2000a) for J, H, K and V-band magnitudes.

| Parameter	Unit	Value
$T_{\rm eff}$	[K]	7750 ± 250
log(g)	[dex]	4.0 ± 0.5
[Fe/H]	[dex]	-0.25 ± 0.5
$v \sin(i)$	[km s^{-1}]	20 ± 10
distance	[pc]	83.8 ± 2.9^a
Age	[Myr]	17 ± 2
$L_\star$	[$L_\odot$]	5.7 ± 1.7
$M_\star$	[$M_\odot$]	1.6 ± 0.1
V	[mag]	7.36 ± 0.01
J	[mag]	6.906 ± 0.019
H	[mag]	6.867 ± 0.047
K	[mag]	6.789 ± 0.021

Notes. $^{(a)}$The HIPPARCOS new reduction from van Leeuwen (2007) gives a significantly different distance of 90.4 ± 3.4 pc.

83.8 ± 2.9 pc (Gaia Collaboration 2016) and with an age estimate of approximately 17 Myr (see main stellar properties in Table 1). This star is known to harbor a debris disk with a high fractional luminosity, 1.5×10^{-3}, derived from IR and submm observations (Nilsson et al. 2010; Rizzuto et al. 2012; Chen et al. 2012). Moór et al. (2013) did not detect any CO emission using APEX and set an upper limit for the total CO mass between 1.4×10^{-4} and 1.7×10^{-4} $M_\oplus$, excluding the possibility of an evolved gaseous primordial disk (in agreement with Kral et al. 2017 secondary gas model predicting a CO mass content of 10^{-5} $M_\oplus$). The disk was resolved with *Herschel* PACS observations. Moór et al. (2013) identified in the deconvolved images at 70 and 100 μm, a large disk structure with a characteristic size fitted by an elliptical Gaussian of 540×490 au ($6.0 \times 5.4''$) with an inclination of $25°$ at a position angle of $105°$. The modeling of the spectral energy distribution (SED) combining 2MASS, IRAS, WISE, *Spitzer*, *Herschel* photometry led them to favor a two-belt architecture with a warm inner belt (187 ± 26 K at 5.9 ± 1.6 au) and a colder outer belt (57 ± 1.5 K at 63.7 ± 4.4 au) that would extend up to 270 au to match the resolved PACS images. The revised values considering the new *Gaia* DR1 distance of HD 95086 remain within the previous uncertainty. Subsequent re-analysis by Su et al. (2015) confirmed the presence of warm and cold belts at the location derived by Moór et al. (2013) using either flat or Gaussian disk models in their SED analysis. It also led them to favor a three-component model with the presence of an additional broad low-eccentricity ($e < 0.3$) disk halo component extending up to 800 au to reconcile SED fitting and their new analysis of the PACS far-infrared resolved images. They also suggest the presence of a closer hotter belt at ~300 K in the terrestrial planet zone (that would be located at ~2 au) or the presence of a weak silicate feature emitted by μm-size grains located in the warm belt to explain the excess of flux in the SED shortward of 10 μm. They also report the detection of 69 μm crystalline olivine feature from the disk as being not spectrally resolved and contributing to ~5% of the total dust mass.

Very recently, Su et al. (2017) resolved for the first time the cold belt with ALMA 1.3 mm observations obtained in January and April May 2015. The disk emission is consistent with a broad ($\Delta R/R \sim 0.84$), inclined ($30° \pm 3°$) ring peaked at 200 ± 6 au from the star. For a two-boundary model, the cold belt is well described with sharp boundaries from 106 ± 6 au to 320 ± 20 au and a surface density distribution described by a power law with an index of -0.5 ± 0.3. The deep ALMA map also reveals the presence of two sources near the edge of the cold belt. The brightest one, however, has a constructed SED consistent with the one expected from a $z = 2$ dusty galaxy. Finally, the disk multi-belt architecture led Su et al. (2015, 2017) to discuss the existence of additional planets around HD 95086 (single to multiple system) considering the properties of HD 95086 b and dynamical constraints from the debris disk distribution and the stability of multiplanetary system configurations.

In 2012, in the course of a thermal angular differential imaging survey of young, nearby intermediate-mass stars (Rameau et al. 2013a), Rameau et al. (2013b) observed the system with NaCo at the Very Large Telescope (VLT). They discovered a very red candidate located at about 620 mas (51.9 au at 83.8 pc) from the star and with a luminosity compatible with a young 4–5 $M_{\rm Jup}$ planet. Subsequent observations in 2013 in the K-band and L'-band enabled confirmation of the common proper motion of the planetary candidate with HD 95086 (Rameau et al. 2013a). Further characterization obtained with NaCo at VLT, NICI and during the early science phase of GPI at Gemini-South confirmed the late-L type and planetary nature of HD 95086 b (Rameau et al. 2013c; Meshkat et al. 2013; Galicher et al. 2014). More recently, De Rosa et al. (2016) reported photometric H (1.5–1.8 μm) and $K1$ (1.9–2.2 μm) spectroscopic observations of HD 95086 b with GPI. They confirm the L-type dusty atmosphere of this giant planet as evidenced by a featureless low-resolution spectrum and a monotonically increasing pseudo-continuum in $K1$ consistent with a cloudy atmosphere. In a complementary study, Rameau et al. (2016) focused their analysis on the system architecture combining NaCo and GPI observations between 2012 and 2016. In that study, the orbital motion of the planet was resolved. The authors report orbital solutions that favor, with 68% confidence, a semimajor axis of 61.7 au (57.2 at 83.8 pc) and an inclination of $153.0°$ for eccentricities smaller than 0.21. They further constrain the presence of inner planets in the system considering the new GPI detection limit performances together with previous NaCo L'-band observations.

Despite the increasing interest in this system in recent years, several fundamental questions remain unanswered regarding the origin and architecture of the debris disk (owing to the limited amount of spatial information), its connection to the presence of HD 95086 b and additional planets in the system or the formation and the physical properties of HD 95086 b itself. To further characterize this young planetary system, in this paper we present a combined exploration using the HARPS and SPHERE observations. We aim to explore the global environment of HD 95086 including the giant planet HD 95086 b, the presence of additional planets from a few stellar radii up to 800 au and the debris disk architecture. We report in Sect. 2 the observing set-up and strategies, as well as the data reduction with the two instruments. In Sect. 3, we report the study of all detected point-sources with SPHERE in the close vicinity (~10–800 au) of HD 95086. In Sect. 4, we present the combined astrometric results obtained with NaCo and SPHERE to derive the best orbital solution for the planet. In Sect. 5, we report the first detection of HD 95086 b in J-band and analyze the spectral energy distribution of the planet together with the published photometry and spectrum
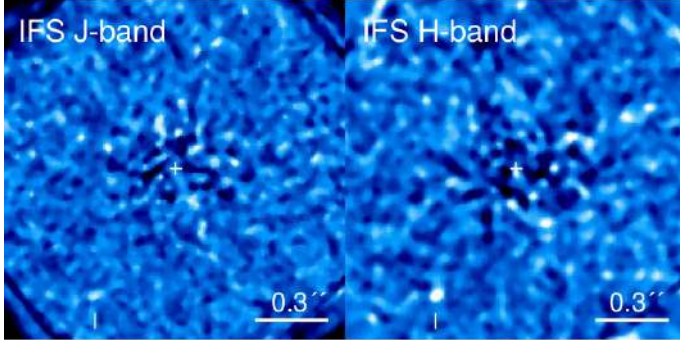
Fig. 1. *Left*: IFS *J*-band image of HD 95086 from a spectral PCA analysis of the combined IFS-YH datacubes obtained in February 2015, May 2015, January 2016 and May 2016. The planet is not detected in the individual epochs and marginally with a S/N of ~3 considering the combination of all epochs. *Right*: same for *H*-band. The planet is detected with a S/N of ~5 considering the combination of all epochs.

from the literature. In Sect. 6, we combine HARPS and SPHERE detection limits to constrain the presence of additional giant planets in that system at short and long periods. In Sect. 7, we report the low signal-to-noise ratio (S/N) detection of the cold outer disk in polarized intensity located at a distance consistent with the debris disk architecture reported by the analysis of the SED and *Herschel* far-IR images, and the recent ALMA 1.3 mm resolved observations. Finally, in Sect. 8, we discuss the global system architecture in the view of our results to investigate the origin of the inner belt and the presence of additional planets in viable dynamical configurations.

2. Observations and data reduction

2.1. VLT/SPHERE Guaranteed time observations

The SPHERE planet-finder instrument installed at the VLT (Beuzit et al. 2008) is a highly specialized instrument, dedicated to high-contrast imaging and spectroscopy of young giant exoplanets. It is based on the SAXO extreme adaptive optics system (Fusco et al. 2006; Petit et al. 2014; Sauvage et al. 2010), which controls a deformable mirror with 41×41 actuators, and four control loops (fast visible tip-tilt, high-orders, near-infrared differential tip-tilt, and pupil stabilization). The common path optics employ several stress-polished toric mirrors (Hugot et al. 2012) to transport the beam to the coronagraphs and scientific instruments. Several types of coronagraphic devices for stellar diffraction suppression are provided, including apodized pupil Lyot coronagraphs (Soummer 2005) and achromatic four-quadrant phase masks (Boccaletti et al. 2008). The instrument has three science subsystems: the infrared dual-band imager and spectrograph (IRDIS, Dohlen et al. 2008), an integral field spectrograph (IFS; Claudi et al. 2008) and the Zimpol rapid-switching imaging polarimeter (ZIMPOL; Thalmann et al. 2008).

2.1.1. Simultaneous integral field spectroscopy and dual-band imaging

As part of the SpHere INfrared survey for Exoplanets (SHINE, Chauvin et al. 2017b) GTO campaign (095.C-0298, 096.C-0241, 097.C-0865, and 198.C-0209), aimed at the detection and characterization of extrasolar planets in the near infrared, HD 95086 was observed at five epochs on February 3rd, 2015, May 5th,

2015, January 18th, 2016, May 31st, 2016, and May 10th, 2017. The data were acquired in IRDIFS-EXT mode, using IRDIS in the dual-band imaging (DBI, Vigan et al. 2010) mode with K_1K_2 filters ($\lambda_{K_1} = 2.1025 \pm 0.1020, \mu m - \lambda_{K_2} = 2.2550 \pm 0.1090, \mu m$), and IFS in the $Y - H$ (0.97–1.66 μm) mode in pupil-tracking. This combination enables the use of angular and/or spectral differential imaging techniques to improve the contrast perfomances at the subarcsecond level.

The standard SHINE observing sequence is composed of one PSF subsequence registered with a series of off-axis unsaturated images obtained with an offset of ~0.4″ relative to the coronagraph center (produced by the tip-tilt mirror) and a neutral density (here ND1.0, which reduces the flux by a factor of ten to avoid saturation)[1]. During this observation, the AO visible tip-tilt and high-order loops remain closed to provide a diffraction-limited PSF. This subsequence is followed by a "star center" coronagraphic observation where four symmetric satellite spots are created by xplucing a periodic modulation on the deformable mirror. They are produced by the SAXO high-order deformable mirror which creates a bidimensional wave and are located at a separation of $14.2 \times \lambda/D$ with adjustable intensity and for two hardcoded configurations (vertically and horizontally aligned as a cross or along the diagonals (see Langlois et al. 2013). The four satellite spots enable an accurate determination of the star position behind the coronagraphic mask for the following deep coronagraphic sequence. Here we used the smallest apodized Lyot coronagraph (ALC-YH-S) with a focal-plane mask of 185 mas in diameter. The deep coronagraphic subsequence that follows typically lasts 1.5–2.0 h. The full sequence is then concluded with a new "star center" sequence, a new PSF registration, as well as a short sky observing sequence for fine correction of the hot pixel variation during the night. For February 3rd, 2015, May 31st, 2016, and May 10th, 2017 the deep coronagraphic sequences were continuously obtained with the four satellite spots to accurately control the stellar position. The observing settings and conditions of all epochs are compiled in Table 2. The January 18th, 2016 observations suffered from low-wind effect (Sauvage et al. 2016) as illustrated in the enlarged image of Fig. 2 degrading the XAO correction and SPHERE performances.

To calibrate the IRDIS and IFS dataset on sky, the astrometric field 47 Tuc was observed. The platescale and true north solution at each epoch is reported in Table 3 based on the long-term analysis of the GTO astrometric calibration described by Maire et al. (2016). The rotation correction considered to align images to the detector vertical in pupil-tracking observations is $-135.99 \pm 0.11°$. Anamorphism correction is obtained by stretching the image Y-direction with a factor of 1.0060 ± 0.0002. All IRDIS and IFS datasets were reduced using the SPHERE Data Reduction and Handling (DRH) automated pipeline (Pavlov et al. 2008) at the SPHERE Data Center (SPHERE-DC) to correct for each datacube for bad pixels, dark current, flat field, and sky background. After combining all datacubes with an adequate calculation of the parallactic angle for each individual frame of the deep coronagraphic sequence, all frames are shifted at the position of the stellar centroid calculated from the initial star center position. For May 5th, 2015, and January 18th, 2016, the determination of the stellar position before and after the deep coronagraphic was used to control the centering stability. A centroid variation of 0.2 pixels at both epochs was derived and quadratically added for the final astrometric

---

[1] https://www.eso.org/sci/facilities/paranal/instruments
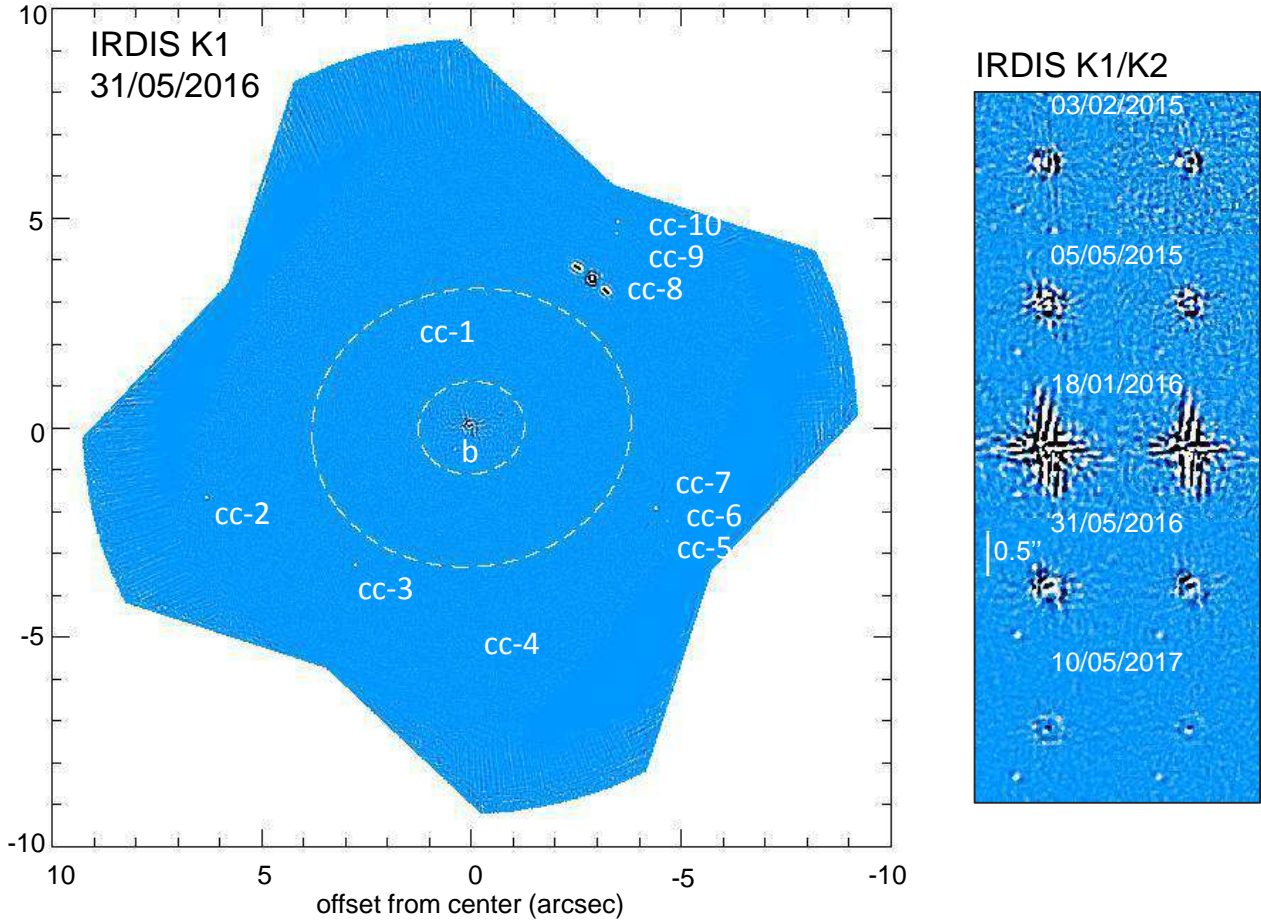
Fig. 2. *Left*: IRDIS *K*1-band full-combined image of HD 95086 from May 31st, 2016. All companion candidates have been marked. HD 95086 b is well detected at a separation of 622 ± 3 mas and position angle of 147.5 ± 0.3 deg from HD 95086. The sharp boundaries at 106 and 320 au of the cold outer belt resolved by ALMA are reported in the IRDIFS FoV (dashed line). *Right*: zoom-in of IRDIS *K*1 and *K*2-band images of HD 95086 and HD 95086 b observed in 3rd February, 2015, May 5th, 2015, January 18th, 2016, May 31st, 2016, and May 10th, 2017. The January 18th, 2016 observations suffered from low-wind effect as shown by the increased level of residuals.

Table 2. Observation log of VLT/SPHERE.

UT Date	Instrument	Mode	Filter	NDIT × DIT[a] (s)	N_{exp}^a	$\Delta\pi^a$ (°)	ω^a (″)	Strehl @1.6 μm	Airmass
03-02-2015	IRDIS	DBI	K1K2	4 × 16	26	17.5	0.58	0.85	1.39
03-02-2015	IFS	$R_\lambda = 30$	YH	1 × 64	26				
02-05-2015	IRDIS	DPI	J	2 × 32	76[c]	–	0.72	0.73	1.40
04-05-2015	IFS	$R_\lambda = 30$	YH	4 × 64	13				
18-01-2016[b]	IRDIS	DBI	K1K2	5 × 64	19	28.4	1.56	0.61	1.39
18-01-2016[b]	IFS	$R_\lambda = 30$	YH	5 × 64	19				
31-05-2016	IRDIS	DBI	K1K2	10 × 64	7	25.3	0.64	0.82	1.41
31-05-2016	IFS	$R_\lambda = 30$	YH	10 × 64	7				
10-05-2017	IRDIS	DBI	K1K2	10 × 64	12	36.6	0.89	0.85	1.39
10-05-2017	IFS	$R_\lambda = 30$	YH	10 × 64	12				

Notes. [a]NDIT refers to the number of integration per datacube, DIT to the integration time, N_{exp} to the number of datacubes, $\Delta\pi$ to the parallactic angle variation during the sequence and ω to the seeing conditions. [b]January 18th, 2016 observations suffered from low-wind effect as illustrated in the enlarged image of Fig. 2. [c]For DPI, we note that one HWP or polarimetric cycles is composed of four data cubes. Twenty cycles were obtained for HD 95086 leading to a total of 76 exposures as one poor-quality cycle was discarded.

budget at each specific epoch. For the February 3rd, 2015, May 31st, 2016, and May 10th, 2017 datasets, we took advantage of the waffle-spot registration to apply a frame-to-frame recentering. The SPHERE-DC corrected products were used as input

to the SHINE *Specal* pipeline which applies flux normalization including the coronagraph transmission correction, followed by different angular and spectral differential imaging algorithms (Galicher et al. in prep). After a Fourier spatial filtering that

Table 3. IRDIS Relative astrometry and photometry of HD 95086 A and b.

| UT Date	Ins-filter	$\Delta\alpha$ (mas)	$\Delta\delta$ (mas)	Sep. (mas)	PA (°)	Contrast (mag)	True north (deg)	Platescale (mas)	Ref.
12-01-2012	NaCo-L'	294 ± 8	-550 ± 8	624 ± 8	151.9 ± 0.8	9.8 ± 0.4	-0.57 ± 0.10	27.11 ± 0.06	1
14-03-2013	NaCo-L'	305 ± 13	-546 ± 13	626 ± 13	150.8 ± 1.3	9.7 ± 0.6	-0.58 ± 0.10	27.10 ± 0.03	1
27-06-2013	NaCo-L'	291 ± 8	-525 ± 8	600 ± 11	151.0 ± 1.2	9.2 ± 0.8	-0.65 ± 0.10	27.10 ± 0.04	1
10-12-2013	GPI-K_1	301 ± 5	-541 ± 5	619 ± 5	150.9 ± 0.5	12.1 ± 0.5	-0.10 ± 0.13	14.166 ± 0.007	2,3
11-12-2013	GPI-H	306 ± 11	-537 ± 11	618 ± 11	150.3 ± 1.1	13.1 ± 0.9	-0.10 ± 0.13	14.166 ± 0.007	2,3
13-05-2014	GPI-K_1	307 ± 8	-536 ± 8	618 ± 8	150.2 ± 0.7	–	-0.10 ± 0.13	14.166 ± 0.007	3
06-04-2015	GPI-K_1	322 ± 7	-532 ± 7	622 ± 7	148.8 ± 0.6	–	-0.10 ± 0.13	14.166 ± 0.007	3
08-04-2015	GPI-K_1	320 ± 4	-533 ± 4	622 ± 4	149.0 ± 0.4	12.2 ± 0.2	-0.10 ± 0.13	14.166 ± 0.007	3,4
29-02-2016	GPI-H	330 ± 5	-525 ± 5	621 ± 5	147.8 ± 0.5	13.7 ± 0.2	-0.10 ± 0.13	14.166 ± 0.007	3,4
06-03-2016	GPI-H	336 ± 3	-521 ± 3	620 ± 5	147.2 ± 0.5	–	-0.10 ± 0.13	12.166 ± 0.007	3
03-02-2015	IRDIS-K_1	322 ± 4	-532 ± 4	622 ± 4	148.8 ± 0.4	12.2 ± 0.1	1.75 ± 0.10	12.26 ± 0.01	5
03-02-2015	IRDIS-K_2	319 ± 5	-532 ± 5	620 ± 5	149.0 ± 0.5	11.8 ± 0.2	1.75 ± 0.10	12.26 ± 0.01	5
05-05-2015	IRDIS-K_1	324 ± 7	-531 ± 7	622 ± 7	148.6 ± 0.6	12.4 ± 0.3	1.75 ± 0.10	12.26 ± 0.01	5
05-05-2015	IRDIS-K_2	322 ± 8	-530 ± 8	620 ± 8	148.7 ± 0.6	12.0 ± 0.3	1.75 ± 0.10	12.26 ± 0.01	5
18-01-2016	IRDIS-K_1	327 ± 8	-531 ± 8	624 ± 8	148.4 ± 0.7	12.2 ± 0.4	1.74 ± 0.10	12.26 ± 0.01	5
18-01-2016	IRDIS-K_2	326 ± 10	-534 ± 10	626 ± 10	148.6 ± 0.9	11.9 ± 0.4	1.74 ± 0.10	12.26 ± 0.01	5
31-05-2016	IRDIS-K_1	334 ± 3	-525 ± 3	622 ± 3	147.5 ± 0.3	12.3 ± 0.2	1.72 ± 0.10	12.26 ± 0.01	5
31-05-2016	IRDIS-K_2	332 ± 4	-523 ± 4	620 ± 4	147.6 ± 0.4	11.8 ± 0.2	1.72 ± 0.10	12.26 ± 0.01	5
10-05-2017	IRDIS-K_1	343 ± 3	-521 ± 3	624 ± 3	146.6 ± 0.3	12.3 ± 0.2	1.78 ± 0.10	12.26 ± 0.01	5
10-05-2017	IRDIS-K_2	343 ± 4	-524 ± 4	626 ± 4	146.8 ± 0.4	12.3 ± 0.2	1.78 ± 0.10	12.26 ± 0.01	5

Notes. (1) Astrometric and photometric results from Rameau et al. (2013b) with the true north recalibrated on the 47 Tuc SHINE reference field ($+0.2 \pm 0.1°$) and the proper motion and precession correction applied for the parallactic angle calculation ($-0.15 \pm 0.05°$). See Appendix A. (2, 3) Astrometric results processed by Rameau et al. (2016) and photometric results from Galicher et al. (2014), respectively. (4) Photometric results reported by De Rosa et al. (2016). (5) This work. Plate scale and true north from Maire et al. (2016) (considering that Maire et al. 2016 report the IRDIS true north correction and not the true north).

removed low-spatial frequencies, the TLOCI (Marois et al. 2014) and PCA (Soummer et al. 2012) algorithms were specifically applied to both IRDIS and IFS data. To attenuate the signal, the *Specal* TLOCI implementation locally subtracts the stellar speckle pattern for each frame in annuli of $1.5 \times FWHM$ further divided in sectors. The subtraction is based on a linear combination of the best 20 (N parameter) correlated reference images calculated in the optimization region and selected to minimize the self-subtraction at maximum 20% (τ parameter). Please refer to Galicher & Marois (2011) and Marois et al. (2014) for further description of the reference frame selection, and the subtraction and optimization regions. For IRDIS, the Specal PCA uses each frame subtracted from its average over the field of view (FoV) to estimate the principal components. The first five components are considered for the final subtraction. For IFS, the spectral diversity is in addition exploited after proper rescaling and renormalization of the IFS datacubes as detailed by Mesa et al. (2015). The first 100 principal components are subtracted. Unlike Specal, the IPAG-ADI pipeline (Chauvin et al. 2012), used to extract the early NaCo astrometric and photometric measurements of HD 95086 b (Rameau et al. 2013a,b), was run with the sADI and PCA algorithms to obtain a consistency check. Astrometric, photometric, and detection limit results were estimated using injected fake planets and planetary signature templates to take into account any biases related to the data processing. The IFS images in J and H-bands are shown in Fig. 1. The full FoV IRDIS image of May 31st, 2016 is shown in Fig. 2 together with the IRDIS K_1 and K_2 subimages of HD 95086 b obtained at each epoch.

2.1.2. Polarimetric differential imaging

On May 2nd, 2015, as part of the DISK GTO program (095.C-0273), a standard differential polarimetric imaging (DPI, Langlois et al. 2014) sequence of HD 95086 was obtained in the *J*-band to possibly detect and study the spatial distribution of small dust grains in the disk surface layers through their scattered light (Kuhn et al. 2001). The debris disk around that source has never been resolved at visible or near-infrared wavelengths. The small Apodized-Lyot coronagraph (ALC-YJ-S) was used with a focal-plane mask of 145 mas in diameter. In DPI mode, IRDIS provides two beams, in which wire-grid polarizers are inserted, and lead to ordinary and extraordinary polarization states. The half-wave plate (HWP) that controls the orientation of the polarization is set to four positions shifted by 22.5° in order to construct the classical set of linear Stokes vectors. A total of 76 datacubes of two frames were acquired for a total exposure time of 49 min on source in field stabilized mode. The detail of the observing setup, airmass, and parallactic angle variations are also reported in Table 2.

Two pipelines developed for high-contrast differential polarimetric imaging were used to calculate the Stokes parameters Q and U. The first is based on the double-ratio method (Avenhaus et al. 2014). A complete description of this method is provided in Benisty et al. (2015). The second is based on the double-difference approach and is described in de Boer et al. (2016). Both methods were independently applied to the HD 95086 dataset. Since the scattered light from a circumstellar disk is expected to be linearly polarized in the azimuthal
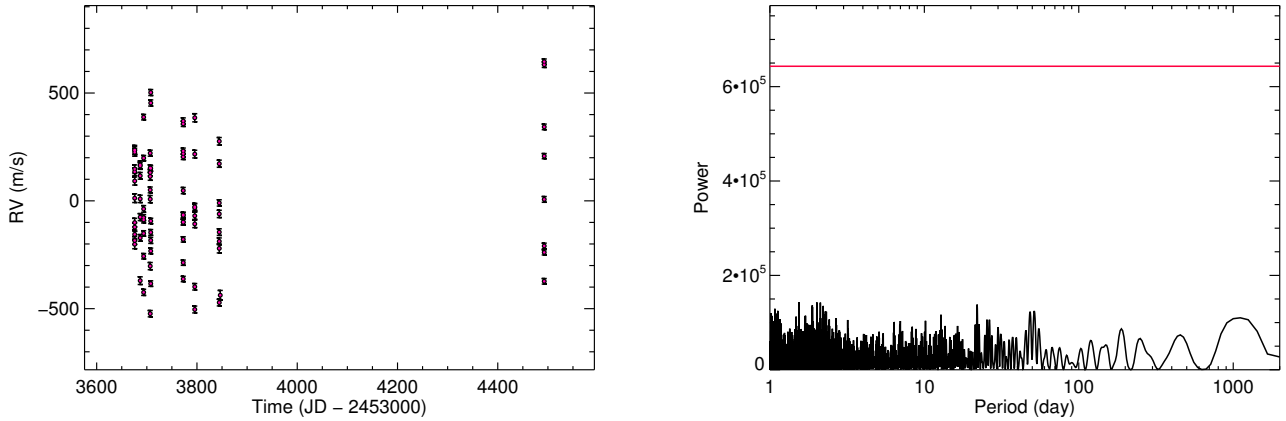
Fig. 3. *Left*: HD 95086 radial velocity variations observed with HARPS with error bars. *Right*: periodogram of HD 95086 radial velocities. The false alarm probabilities at 10% is plotted as a red line. There is no clear detection of significant periodic radial velocity variation in our data.

direction under the assumption of single scattering, it is beneficial to describe the polarization vector field in polar rather than Cartesian coordinates. Once data have been corrected for distortion, true north, and instrumental effects such as the angular misalignment of the HWP, the Q_ϕ, U_ϕ radial polarized Stokes parameters are calculated following the principle of Schmid et al. (2006). In this coordinate system, the azimuthally polarized flux from a circumstellar disk appears as a consistently positive signal in the Q_ϕ image, whereas the U_ϕ image remains free of disk signal and provides a convenient estimate of the residual noise in the Q_ϕ image (Schmid et al. 2006). This assumption is valid for low-inclination optically-thin debris disks (Canovas et al. 2015). The outcome of the observations are discussed in Sect. 7.

2.2. ESO 3.6 m telescope HARPS radial velocity

Between 2014 and 2016, high S/N spectra of the A8V early-type star HD 95086 were obtained with the HARPS spectrograph (Pepe et al. 2002) installed on the 3.6 m ESO telescope at La Silla Observatory (Chile) in the southern hemisphere. These observations were part of two HARPS Open Time and Large Programs (099.C-0205 and 192.C-0224) focused on the search for exoplanets around young, nearby stars. The radial velocities were measured using the dedicated SAFIR code (Galland et al. 2005) based on the Fourier interspectrum method developed by (Chelli 2000). A reference spectrum (average of all spectra) was used instead of a classical binary mask for cross-correlation and estimation of the radial velocity data. This reference spectrum offers the possibility of applying a differential approach based on star spectrum itself and using the low-frequency structures and spectral discontinuities to estimate the best value of the stellar velocity in presence of stellar noise. The application of the Fourier approach to early-type stars that present a small number of stellar lines, usually broadened and blended by stellar rotation, has proven to be very successful for the detection of planets (e.g., Borgniet et al. 2017). The results of the radial velocity variation and periodogram are reported in Fig. 3 and cover a timeline of more than 1000 days. The typical uncertainty associated with HARPS data is of 15 m s^{-1} on average. The observed scatter in the radial velocity variation is one order of magnitude larger than the individual radial velocity uncertainty and is probably due to the presence of pulsations as expected for young, early-type stars with similar spectral types as HD 95086.

3. Point-source identification in the stellar vicinity

In the full IFS FoV ($1.77'' \times 1.77''$), excluding the star, the unique point-source detected is the planet HD 95086 b located at a separation of ~620 mas and position angle of ~148.0° from HD 95086. The IFS photometry and astrometry is discussed in Sects. 4 and 5. In the final IRDIS image (combining all rotated FoVs of $11'' \times 11''$), together with HD 95086 b, ten companion candidates (ccs) are detected as shown in Fig. 2 for the May 31st 2016 epoch. All candidates are identified in the five SHINE epochs with $S/N \geq 10$ (except cc-4 with a S/N of ~5). The cc relative astrometry and photometry with error bars is derived using a standard fake planet injection with a χ^2 minimization of the residuals within a segment of $1 \times FWHM$ extension in radius and $3 \times FWHM$ in azimuth (Chauvin et al. 2012). cc-8 corresponds to the bright background star identified by Rameau et al. (2013b) that served as a sanity-check for the inter-astrometric calibration done between each NaCo observation to confirm the discovery of HD 95086 b. None of the candidates detected correspond to the bright and faint sources resolved by ALMA deep 1.3 mm observations of Su et al. (2017) and located near the edge of the cold outer belt as seen in Fig. 2. Same conclusions are drawn when going back to the NaCo L' deep ADI observations of Rameau et al. (2013b,c).

To control and identify the presence of systematic biases related to the platescale and true north correction in our SPHERE reduction, we measured the relative motion of all ccs (except cc-4) detected with IRDIS. This aspect is critical as uncertainties on the platescale and true north can significantly affect the determination of the relative position of HD 95086 b, although closer than all ccs. A typical true north systematic bias between two epochs of 0.2° would convert into a systematic of 0.2 pixels (2.5 mas) at HD 95086 b's location (~620 mas), that is, the typical uncertainty we aim at with which to monitor the planet's orbital motion given the good S/N (~10) achieved with IRDIS. Such a bias scales into a 1.7 pixels shift for ccs at the edge of the IRDIS FoV which would be easily spotted. In Fig. 4, we report the differences between the relative astrometric positions of all ccs between two SPHERE epochs: between February 3rd, 2015 and May 5th, 2015 (top) and between February 3rd, 2015, and May 31st, 2016 (bottom). The expected variation for stationary background objects is also reported with uncertainties based on the primary parallactic and proper motions. Except for HD 95086 b, all companion candidates are clearly identified as background contaminants. Despite the modest parallactic and
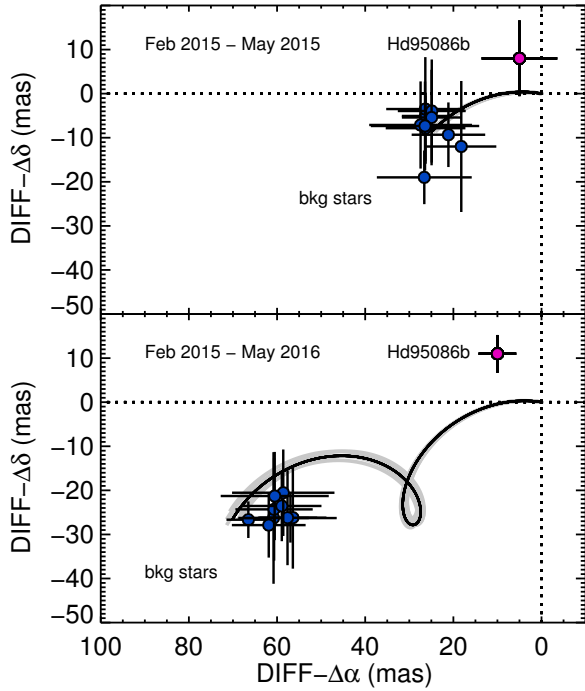
Fig. 4. *Top*: SPHERE/IRDIS relative astrometry differences (dark blue filled circles with uncertainties) of the offset positions of all point-like sources detected in the close vicinity of HD 95086 (see Fig. 2) between May 5th, 2015, and Feb. 3rd, 2015. The expected variation of offset positions, if the candidates are stationary background objects is shown (solid line with uncertainties). The variation is estimated based on the parallactic and proper motions of the primary star, as well as the initial offset position of the companion candidates from HD 95086. The planet position is indicated with a pink circle. Except for HD 95086 b, all companion candidates are clearly identified as background contaminants. *Bottom*: same as top panel but between May 31st, 2016, and Feb. 3rd, 2015.

proper motions of HD 95086, we can see that the companionship confirmation can be obtained with a good level of confidence ($\geq 3\sigma$) in three months owing to the astrometric performances of SPHERE. We can also see that the difference of relative positions of the ccs remain very compact (within ≤ 4 mas) comforting the good platescale and true north astrometric calibration and the corresponding uncertainties (typically 0.1° on the true north for each individual epoch). This verification was applied at each epoch to control systematic biases related to the platescale and true north correction in our SPHERE reduction. As shown in Fig. 4, small systematic effects are still perceptible but within our error bars. The effects vary from one epoch to another and are likely imputable to the nonsimultaneity of the science and astrometric calibration observations or to residual errors related to atmospheric and instrumental limitations.

4. Orbital properties of HD 95086 b

4.1. Relative astrometry

Similarly to all ccs detected in the IRDIS FoV, the relative astrometry and photometry of HD 95086 b was obtained in K_1 and K_2-bands using a standard fake planet injection with a χ^2 minimization of the residuals within a segment of 1 *FWHM* extension in radius and 3 *FWHM* in azimuth (see Chauvin et al. 2012). The averaged PSFs from the start and end subsequences were used for injection. The results for each filter and epochs are reported in Table 3. IRDIS results at all epochs were found

Table 4. IFS Relative astrometry and photometry of HD 95086 A and b.

| Ins-Filter	$\Delta\lambda$ (μm)	Sep. (mas)	PA (°)	Contrast (mag)
J_{IFS}	1.20–1.32	627 ± 6	147.9 ± 0.5	$14.5^{+0.5}_{-0.4}$
H_{IFS}	1.60–1.65	626 ± 8	147.8 ± 0.7	13.7 ± 0.3

consistent between the IPAG-ADI pipeline using sADI and PCA and the SHINE *Specal* pipeline using TLOCI and PCA. They are reported together with the NaCo relative astrometry of HD 95086 b obtained on January 12th, 2012, March 14th, 2013 and June 27th, 2013. The IFS astrometric results are reported in Table 4. They are consistent with the IRDIS results and are not considered in the following analysis given their limited S/N and the fact they were obtained from images combining several epochs.

The NaCo astrometry was re-calibrated using contemporaneous observations of the NaCo reference field we used since 2002 for 2M1207, β Pictoris and HD 95086 using the Orion stars TCC054, 58, 57, 34, and 26 (McCaughrean & Stauffer 1994; Chauvin et al. 2012) and the 47 Tuc primary calibrator of SHINE (Maire et al. 2016). These observations were obtained in December 2014. We find a true north correction of $+0.2 \pm 0.1°$ to add to the NaCo astrometry to enable the homogenous calibration of NaCo and IRDIS data on 47 Tuc. Finally, the NaCo astrometry published by Rameau et al. (2013c) was also corrected from a bias of $-0.15 \pm .05°$ related to the nonconsideration of the proper motion and precession correction in the equatorial coordinates of HD 95086 for the parallactic angle calculation. GPI measurements published by Rameau et al. (2016) are reported in Table 3 for comparison and discussion about both instrument astrometric performances. They actually refer to De Rosa et al. (2016) for the platescale and true north solutions determined by continually observing a set of astrometric calibrators with well-determined orbital solutions or contemporaneous NIRC2 measurements. As we cannot exclude at this stage the presence of systematic biases between SPHERE and GPI as our reference calibrators are not the same, we did not consider the GPI results in the following orbital fitting analysis. NaCo, IRDIS, and GPI astrometric results are shown together in Fig. 5. Expected variation of offset positions in case of a background object is reported in red and unambiguously confirms that HD 95086 b is co-moving. The NaCo (re-calibrated) and IRDIS measurements independently confirm that the orbital motion is now resolved with a high level of confidence as reported by Rameau et al. (2016). Although GPI and SPHERE observations were not taken at the same epochs, we can try to link the closest measurements in time. Some small variations can be seen between almost contemporaneous GPI measurements or IRDIS and GPI measurements, but they all remain within the 1σ error bars. They independently demonstrate the unprecented astrometric accuracy (3 mas in the best cases here) and the calibration procedure achieved by the new generation of planet imagers.

4.2. Orbital fitting

As mentioned previously, we considered the NaCo and SPHERE data points only, to exclude any possible systematics in the orbital fitting analysis. Following the method developed for β Pictoris (Chauvin et al. 2012), we used a Markov-chain Monte-Carlo (MCMC) Bayesian analysis technique (Ford 2005, 2006), which is well suited for observations covering a small
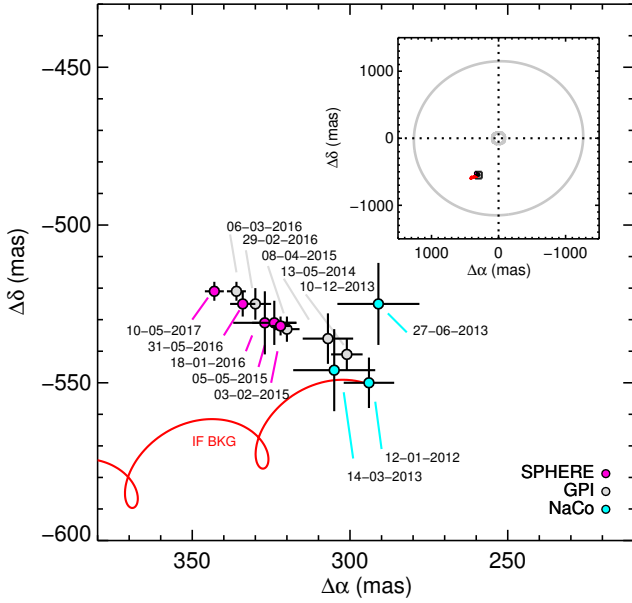
Fig. 5. Astrometric positions of HD 95086 b relative from A. The predictions for the HD 95086 b in case of a stationary background source are reported in red. SPHERE (pink) and GPI (gray) astrometric observations between 2013 and 2017 are reported together with the NaCo observations (light-blue). The inset shows the planet location relative to the ones of the cold outer belt and warm inner belt from Su et al. (2017).

Table 5. MCMC solutions for the orbital parameters of HD 95086 b.

Parameter	Unit	MCMC solutions
a	(AU)	$52.0^{+12.8}_{-24.3}$
P	(yr)	$288.6^{+11.5}_{-176.5}$
e		$0.2^{+0.3}_{-0.2}$
i	(°)	$140.7^{+14.8}_{-13.3}$
Ω	(°)	Peaks at $-31.4 \pm 180°$ and $-118.9 \pm 180°$
ω	(°)	~Flat distribution
t_p	(yr JD)	Peaks at 1933.1 and 2093.0 AD

Notes. Semi-major axis (a), period (P), eccentricity (e), inclination (i), longitude of ascending node (Ω), argument of periastron (ω) and time of periastron passage (t_p).

part of the whole orbit (for large orbital periods). This is the case for HD 95086 b as illustrated in the insert of Fig. 5. We did not consider any prior information on the inclination or longitude of the ascending node to explore the full orbital parameter space of bound orbits. As described in Appendix A of Chauvin et al. (2012), we assumed the prior distribution $p_0(\boldsymbol{x})$ to be uniform in $\boldsymbol{x} = (\log P, e, \cos i, \Omega + \omega, \omega - \Omega, t_p)$ and worked on a modified parameter vector $\boldsymbol{u}(\boldsymbol{x})$ to avoid singularities in inclination and eccentricities and improve the convergence of the Markov chains. The most likely solutions are given in Table 5. The complete results of the MCMC analysis are reported in Fig. 6, together with the results of a classical least-squared linear method (LSLM) flagged by the red line. It shows the standard statistical distribution matrix of the orbital elements a, e, i, Ω, ω, and t_p, where a stands for the semi-major axis, e for the eccentricity, i for the inclination, Ω the longitude of the ascending node (measured from north), ω the argument of periastron and t_p the time for periastron passage.

The results of our MCMC fit indicate orbital distributions that peak with a 68% confidence interval at $52.0^{+12.8}_{-24.3}$ au for the semi-major axis, $140.7^{+14.8}_{-13.3}°$ for the inclination, eccentricities that fall within $e = 0.2^{+0.3}_{-0.2}$. The longitude of ascending node shows several peaks at $\Omega - 31.4 \pm 180°$, $\Omega = -118.9 \pm 180°$, but is not very strongly constrained, as well as the argument of periastron ω. Periastron passages occur between 1800 and 2200 AD with two peaks at 1933.1 and 2093.0 AD. The latter parameters are badly constrained, basically because the set of acceptable orbital solutions is compatible with circular orbits and also with $i = 180°$. Nonetheless, the inclination distribution clearly favors retrograde orbits ($i > 90°$), which is compatible with the observed clockwise orbital motion resolved with NaCo, GPI and SPHERE. The rather loose error bars directly result from the fact that we fit only a very small portion of the whole orbit corresponding to an almost linear orbital variation

described by four parameters (position and velocity in the projected celestial plane) without any constraints in the third spatial dimension (the line of sight). The fact that favored solutions of periastron passages fall at the current epoch likely result from the limited number of observational constraints biasing the orbital fitting process.

Coplanar solutions with the outer belt plane resolved by ALMA ($i_{disk} = 130 \pm 3°$, $\Omega = 97 \pm 3°$, Su et al. 2017) are compatible with the posterior distribution of orbits, although not falling at the current peak of the distribution. We defined them as coplanar when the mutual inclinations between the planet orbital plane and the outer belt plane lie within $\pm 5°$. The mutual inclination (i_{tilt}) is given by

$$\cos(i_{tilt}) = \cos(i)\cos(i_{disk}) + \sin(i)\sin(i_{disk})\cos(\Omega - PA_{disk}). \quad (1)$$

The corresponding coplanar solutions are shown in Fig. B.1. They favor an orbit with lower eccentricities and smaller semi-major axis. If we exclude in addition all coplanar solutions for which an outer extent of the chaotic zone created by HD 95086 b lies below 10 au or beyond 106 au (following Lazzoni et al. 2018 prescriptions), we restrain even more the (a, e) parameter space compatible with our NaCo and SPHERE observations, and the inner edge of the cold outer belt as seen in Fig. 7).

Globally, our orbital fitting analysis is consistent with the results of (Rameau et al. 2016, see their Table 1 and Fig. 3 considering a correction factor of 0.92 in sma and 0.89 in period given the new *Gaia* distance), although less constraining regarding the values within the 68% confidence interval. Both favor retrograde low- to moderate-eccentricity solutions with semi-major axes peaking at 50–55 au that are compatible within the error bars with a coplanar configuration with the disk inclination. The small differences between Rameau et al. (2016) and this work may arise from the incomplete overlap in terms of values and uncertainties between SPHERE and GPI in addition to the new *Gaia* distance revision. To verify the possible discrepancies due to the use of different MCMC orbital fitting approaches in this work (Beust et al. 2016) and by Rameau et al. (2016) refering to the Orbits For Impatients Tools (OFTI) developed by (Blunt et al. 2017), we ran as a check our MCMC analysis on the same set of NaCo and GPI data used by Rameau et al. (2016). The results are presented in Fig. C.1, and can be compared with Fig. 3 of Rameau et al. (2016). There is a very good match between the distributions of parameters found by both tools. We see some minor variations for the eccentricity
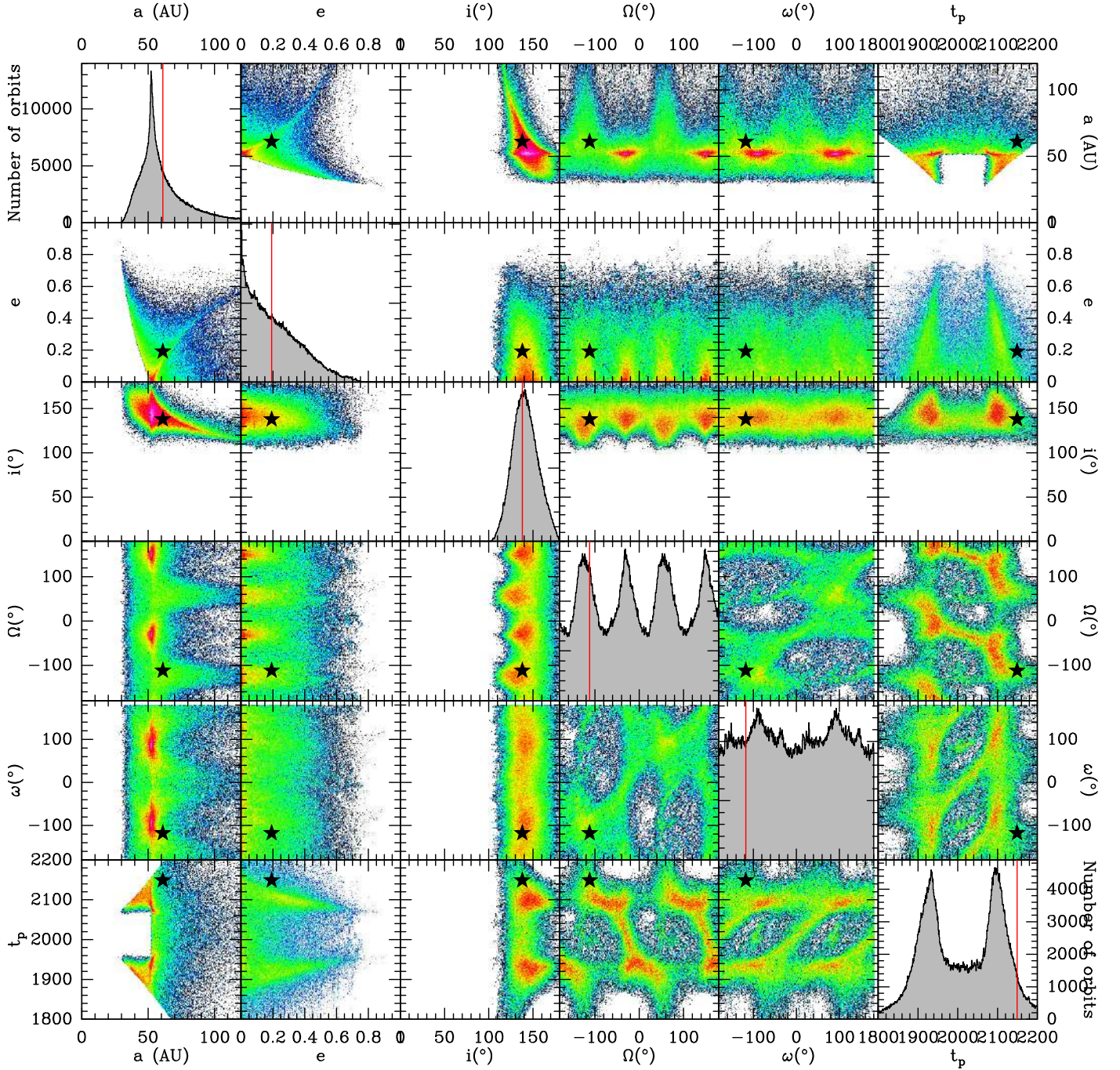
Fig. 6. Results of the MCMC fit of the NaCo and SPHERE combined astrometric data of HD 95086 b reported in terms of statistical distribution matrix of the orbital elements a, e, i, Ω, ω, and t_p. The red line in the histograms and the black star in the correlation plots indicate the position of the best LSLM χ_r^2 model obtained for comparison.

distribution possibly linked to the difference of prior, and for the distribution of time of periastron passage probably related to the nonrenormalization of the distribution by Rameau et al. (2016) over a given range of orbital period.

5. Spectral energy distribution of HD 95086 b

5.1. Conversion to fluxes

We used a spectral template from the BT-NEXTGEN library (Allard et al. 2012) degraded to $R \sim 30$ (the smallest resolution of our new observations) and adjusted it onto the TYCHO B and V,

2MASS J, H, K_s, and WISE $W1$ and $W2$ photometry (Høg et al. 2000b; Cutri et al. 2003; Cutri et al. 2012). The star photometry is best represented by a model with $T_{\rm eff} = 7600$ K, and $\log(g) = 4.0$. We assumed a metallicity of [M/H] = 0 supported by the abundance analysis of a few LCC members by Viana Almeida et al. (2009). Those parameters are close to those found by Moór et al. (2013) and considered by De Rosa et al. (2016). The fit is shown in Fig. A.1. We used this spectrum to compute the average stellar flux at the wavelengths of the $J_{\rm IFS}$ and $H_{\rm IFS}$ SPHERE IFS passbands (Table 4), and through the IRDIS $K1$ and $K2$, and GPI H and $K1$ IFS passbands. In addition to the SPHERE IFS relative photometry of Table 4, we took the weighted mean of the GPI H
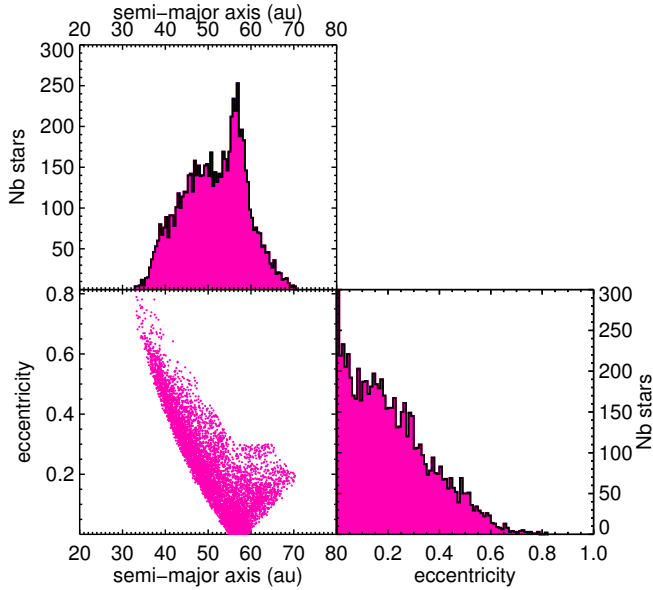
Fig. 7. Orbital solution of HD 95086 b assuming a coplanar configuration with the outer belt inclination ($i_{disk} = 130 \pm 3°$, $\Omega = 98 \pm 3°$, Su et al. 2017), an inner extent of the chaotic zone larger than 10 au, and an outer extent of the chaotic zone smaller than 106 au, that is, the inner boundary of the outer belt resolved by ALMA 1.3 mm observations.

and $K1$, SPHERE $K1$, and SPHERE $K2$ contrast values reported in Table 3 to compute the photometry of HD95086 b into the corresponding passbands. SPHERE and GPI passbands do overlap at H and K-band, but do not cover the same spectral range. They were therefore independently considered for the spectral analysis. Finally, we considered the remaining flux values from low resolution GPI $K1$ spectrum and NaCo L' photometry of Table 1 of De Rosa et al. (2016).

5.2. Color-magnitude diagrams

We report in Fig. 8 the location of HD95086 b in the J-band and K-band based color-magnitude diagrams (CMD). Details of the diagrams are given in Mesa et al. (2016) and Samland et al. (2017). We used here the most recent parallaxes of the young objects from Liu et al. (2016), and included additional companions (Gauza et al. 2015; Stone et al. 2016b; De Rosa et al. 2014) at the L/T transition, and/or members of Sco-Cen (Lachapelle et al. 2015; Bailey et al. 2014; Wagner et al. 2016, and ref. therein). HD 95086 b falls at the L/T transition but is underluminous compared to the field dwarfs. The underluminosity is characteristic of young L/T objects (see Fig. 25 of Liu et al. 2016, and ref. therein). Its placement is marginally consistent in both diagrams with VHS J125601.92-125723.9 ABb (age ≤ 320 Myr, L7, Gauza et al. 2015) if the distance to the system is 12.7 pc (Stone et al. 2016b). The planet has a photometry compatible with that of the peculiar L9 dwarf WISE J164715.57+563208.3 (Appendix C; assuming that the parallax reported in Kirkpatrick et al. 2011 is robust). The latter has recently been proposed to be a 4–5 M_{Jup} free-floating member of the Argus association, that is, an object with a mass in the same range as HD 95086 b. To conclude, the planet falls in the K1–K2 diagram close to HR 8799b and WISE0754+49, two objects with early T spectral types and red colors. HR 8799b has a mass close to the one of HD 95086 b (estimated at 4–5 M_{Jup}). We overlaid on the diagrams the reddening vectors caused by interstellar extinction (Draine 2003) and by 0.5 μm forsterite grains which are proposed to explain

the red colors of the dusty and/or variable L dwarfs (Marocco et al. 2014; Bonnefoy et al. 2016; Hiranaka et al. 2016; Lew et al. 2016). For the forsterite grains, we used the optical constants of Scott & Duley (1996). The young and/or dusty L/T object photometry is shifted along those vectors (see Bonnefoy et al. 2016) with respect to the sequence of field dwarfs, and so does HD 95086 b.

5.3. Empirical spectral comparison

We compared the J to K-band spectrophotometry of HD 95086 b to that of comparison objects generated from low resolution ($R_\lambda \sim 75$-120) spectra acquired with the SpeX instrument. The spectra considered were taken from the SpeXPrism library (Burgasser 2014; 532 objects), Best et al. (2015; 122 objects), and Mace et al. (2013; 72 objects). The first two libraries include spectra of peculiar "dusty" L dwarfs. We also considered the spectra of young M and L dwarfs of Allers & Liu (2013; 17 spectra), and of red, dusty L dwarfs later than L4 taken from the literature (see Appendix D). To conclude, we included in the analysis the spectra of the exoplanets HR8799c and d (Oppenheimer et al. 2013; Pueyo et al. 2015; Zurlo et al. 2016), and of the companions younger than the population of field objects and spanning the L/T transition (age ≤ 400 Myr): VHS J125601.92-125723.9 ABb, 2M1207b (Patience et al. 2010), HR8799d and e (Zurlo et al. 2016), HIP203030B (Bonnefoy et al., in prep), ζ Del B (De Rosa et al. 2014), 2M0219-39b (Artigau et al. 2015), 2M0122-24B (Hinkley et al. 2015), and G196-3B (Rebolo et al. 1998).

All spectra were smoothed to a resolution of $R_\lambda \sim 66$, corresponding to the resolution of the GPI spectrum[2]. We considered the G goodness-of-fit indicator defined in Cushing et al. (2008) which accounts for the filter and spectral channel widths to compare each of the k template spectra to the n spectrophotometric datapoints of HD 95086 b

$$G_k = \sum_{i=1}^{n} w_i \left(\frac{f_i - \alpha_k F_{k,i}}{\sigma_i} \right)^2, \tag{2}$$

where f_i and σ_i are the observed data point i and associated error, w_i is the filter width of the corresponding data point. $F_{k,i}$ is the value of the photometry in the given filter passband i or GPI IFS wavelength channel for the template spectrum k. α_k is a multiplicative factor between the planet spectrophotometry and the one of the template which minimizes G_k and is given by

$$\alpha_k = \frac{\sum_{i=1}^{n} w_i f_i F_{k,i}/\sigma_i^2}{\sum_{i=1}^{n} w_i F_{k,i}/\sigma_i^2}, \tag{3}$$

The GPI spectrum is affected by correlated noise (Greco & Brandt 2016). De Rosa et al. (2016) accounted for this noise in the fit

$$G_k = R_k^T C^{-1} R_k + \sum_{i=1}^{n} w_i \left(\frac{f_i - \alpha_k F_{k,i}}{\sigma_i} \right)^2, \tag{4}$$

where C is the correlation matrix determined following Greco & Brandt (2016) and $R_k = f - \alpha_k F_k$. De Rosa et al. (2016) found α_k via a truncated-Newton algorithm. We preferred to find the one minimizing G_k, considering values of α_k plus or minus 100 times

---

[2] The SPHERE and P1640 JH spectra were not smoothed because their original resolution is lower than the one of GPI. Nonetheless, the spectrophotometry of HD 95086 b in the J and H band is lower than the SPHERE and P1640 data.
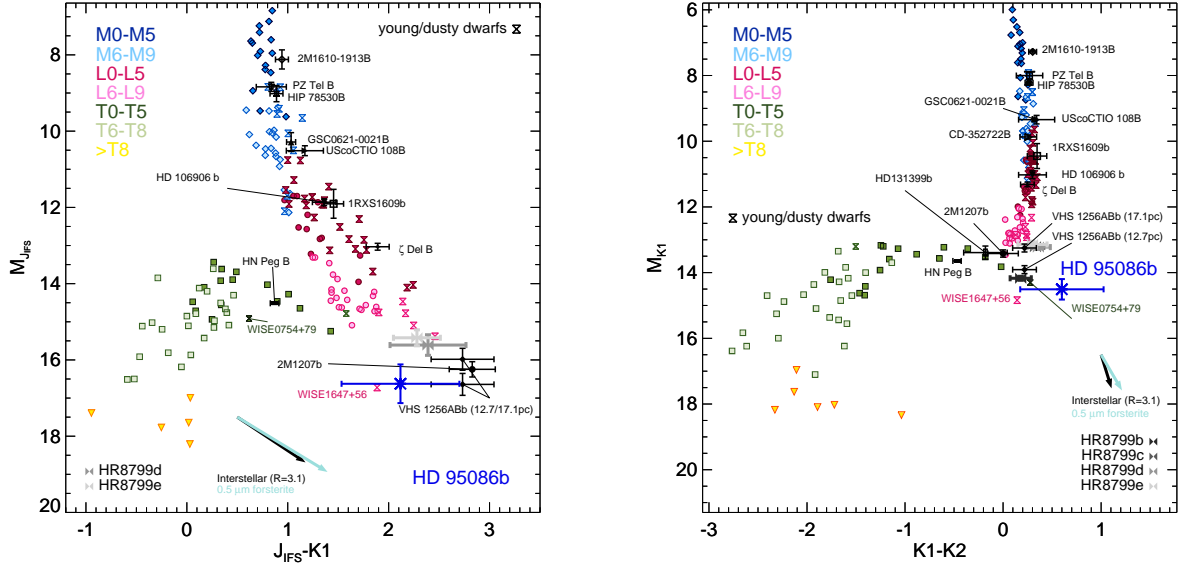
Fig. 8. *Left*: color-magnitude diagram considering the SPHERE/IRDIS $K1$ photometry, and the J_{IFS} photometry from 1.2 to 1.32 μm as it can be extracted from the SPHERE/IFS datacubes. Right: color-magnitude diagram considering the SPHERE/IRDIS $K1$ and $K1$ photometry. In both cases, Measurements of M, L, T field dwarfs, and of young companions and red dwarfs are reported. The reddening vector computed for the synthetic interstellar extinction curve for a 0.5 mag K band extinction and reddening parameter of $R_v = 3.1$ is overlaid (black arrow). We also report the reddening vector from the extinction curve of forsterite dust grains with size distribution centered on radii $r = 0.5\,\mu$m and for a 0.15 mag K band extinction (light blue arrow). As proposed by Marocco et al. (2014) and Bonnefoy et al. (2016), both could explain the deviation of the colors of young and dusty L6–L8 dwarfs, and of the HR 8799 planets with respect to the sequence of field dwarfs. The photometry of HD 95086 b shown by the blue cross with uncertainties in both diagrams is characteristic of young L/T transition objects.

the one found with Eq. (3). This exploration of α_k is sufficient to keep the values of G_k unchanged for all the considered comparison objects.

We show in Fig. 9 the evolution of G with the spectral type for the different libraries of templates considered. We find that the planet photometry is best fitted by dusty and/or young L5-L7.5 dwarfs. Among the SpeXprism library, we retrieve a best fit for the L7 dwarf 2MASSWJ2244316+204343, a candidate member of the AB Dor moving group (see Appendix D). The dusty L/T transition object WISEJ064205.58+410155.5 is the template from the Mace et al. (2013) library which provides the best fit to the planet spectrophotometry. This object is a possible member of the AB Dor moving group (Gagné et al. 2015b). The best fits for the Best et al. (2015) library and among the dusty L dwarfs considered (Appendix D) are obtained for PSO_J057.2893+15.2433 and 2MASS J11193254–1137466, two L7 objects which are candidate members of the β Pictoris moving group and TW Hydrae association, respectively. These objects have predicted masses of 6.6–9.9 and 4.3–7.6 M_{Jup}, respectively (Best et al. 2015; Kellogg et al. 2016). To conclude, we find that the companions HR8799d, 2M1207b, and VHS J125601.92-125723.9 ABb are also reproducing well the spectrophotometry of HD 95086 b.

We compare in Fig. 10 the spectrophotometry of HD 95086 b to some of the best fitting templates. The planet has an H-band flux (SPHERE and GPI) lower than the one of the isolated objects. This discrepancy is slightly reduced for the youngest objects. The companion VHS J125601.92-125723.9 ABb appears to produce the best fit to the 1.2–2.3 μm spectrophotometry of the HD 95086 b. While the peculiar L9 dwarf WISE1647+56 occupies the same location as HD 95086 b in the color-magnitude diagrams (Fig. 8), this object has a bluer spectral slope than the companion.

We compare in Fig. 11 the 1–4 μm spectrophotometry to those of objects with published L' photometry or L-band
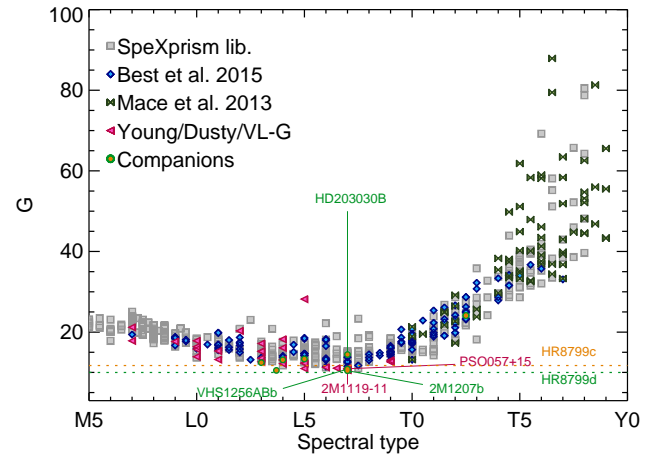
Fig. 9. Evolution of G with the spectral type for the different libraries of comparison objects considered.

spectra (Chauvin et al. 2004; Marois et al. 2008; Stephens et al. 2009; Rich et al. 2016) and known distances (Ducourant et al. 2008; Faherty et al. 2012; Gaia Collaboration 2016; Liu et al. 2016; Gauza et al. 2015; Stone et al. 2016a)[3]. These reference spectra were renormalized following Eqs. (2) and (3) to minimize G when compared to the 1–4 μm spectral energy

---

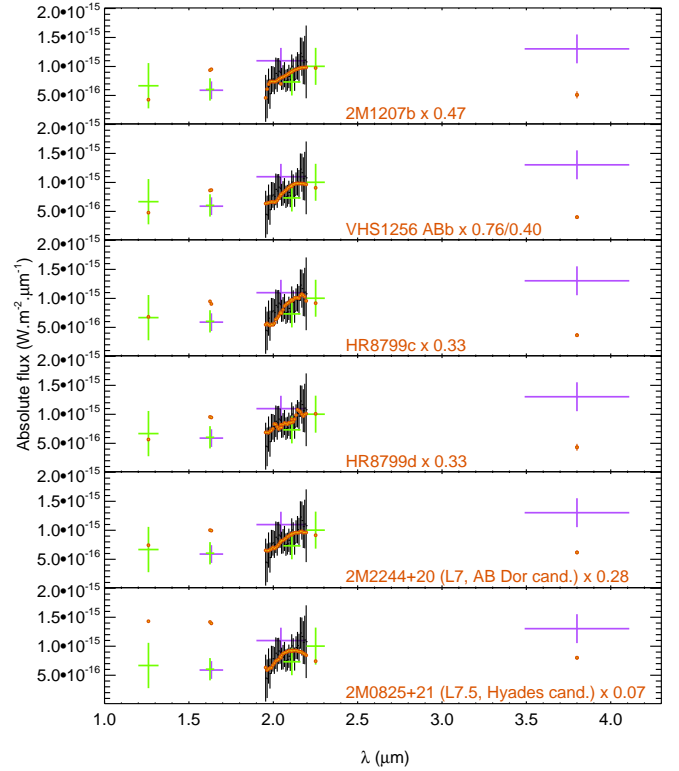[3] De Rosa et al. (2016) performed an analysis which includes many more comparison objects without published L' band photometry. To do so, they converted the WISE 1 magnitude to a L' band magnitude using empirical relations based on the use of empirical spectra from the IRTF Spectral Library and the SpeX Prism Spectral Library. We preferred to avoid using those conversion formulae because the empirical libraries considered to derive them contain mostly spectra of old objects. Yet, the L-band shape is known to be influenced by the age and/or surface gravity (see Stephens et al. 2009; Stone et al. 2016a).
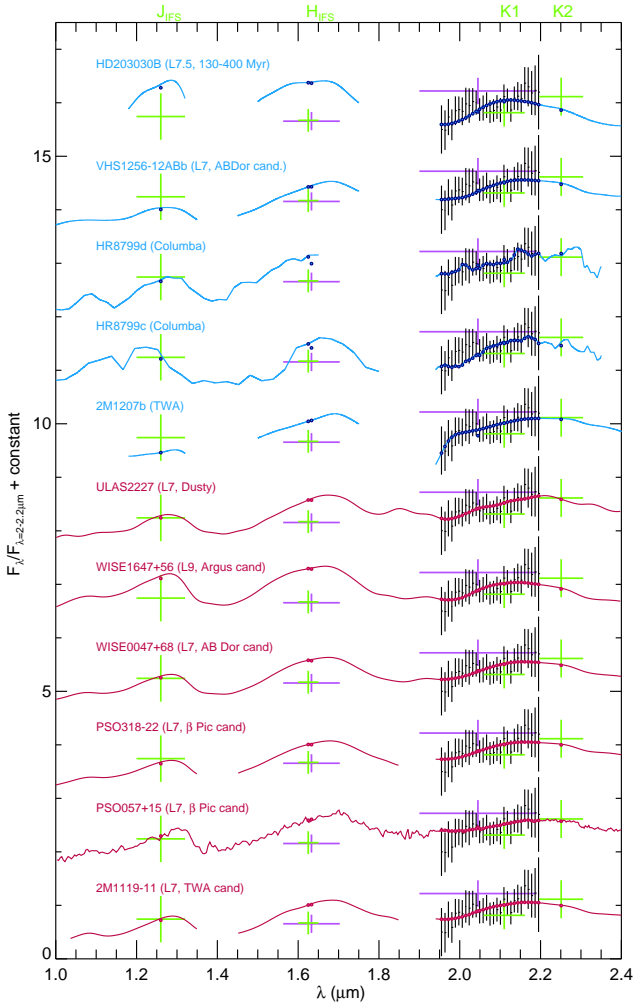
Fig. 10. Spectrophotometry of HD 95086 b (SPHERE IFS J_{IFS}, H_{IFS}, and IRDIS $K1$ and $K2$ photometric datasets in green, GPI H and $K1$ photometric datasets in purple, and GPI low-resolution $K1$ spectrum in black) compared to near-infrared spectra of young and/or dusty L7-L7.5 dwarfs (dark red) and companions (blue) younger than the field. The L7 dwarfs candidate members of young moving groups are sorted by their supposed age.

Fig. 11. 1–4 μm spectral energy distribution of HD 95086 b (SPHERE IFS J_{IFS}, H_{IFS}, and IRDIS $K1$ and $K2$ photometric datasets in green, GPI H and $K1$ photometric datasets in purple, GPI low-resolution $K1$ spectrum in black, and NaCo L' photometric datset in red.) compared to that of young and/or dusty L7-L7.5 dwarfs and companions (dark red) younger than the field.

distribution of HD 95086 b. This comparison confirms that the planet H band flux is fainter compared to the average flux of the templates. In addition, the spectral slope of HD 95086 b is much redder than those objects. This confirms the conclusions of De Rosa et al. (2016). The slope of the 1–4 μm SED of the L7 dwarf 2MASS J22443167+2043433 (AB Dor candidate member) is redder than the one of the L7.5 Hyades candidate member 2MASS J08251968+2115521 (Bannister & Jameson 2007). Since HD 95086 b is much younger than AB Dor, this suggests that its very red slope is the extreme example of the impact of surface gravity on the photospheric opacities. Liu et al. (2016) showed that the underluminosity of young L/T transition objects compared to field objects is more dramatic in the Y, J, and H bands while it is reduced in the K and W1 bands. Because HD 95086 b is an extreme object, we believe that the bolometric corrections, defined by Filippazzo et al. (2015) for the J and K bands and for young objects, are not suitable for the planet and should not be used to derive the luminosity.

In summary, the empirical analysis reveals that the planet 1–2.5 μm photometry is represented by a few empirical objects with estimated spectral types L7–L9, which are candidate members of young moving groups, and whose masses are close to the one estimated for the planet (4–5 M_{Jup}). The extremely red 1–4 μm spectral energy distribution of HD 95086 b and its underluminosity are characteristics of low gravity objects of the L/T transition and render the estimate of the bolometric luminosity uncertain. HD 95086 b probably falls in a regime where the underluminosity related to young objects is maximum, especially at JHK bands where GPI and SPHERE operate. In comparison, HD 95086 b has the same L-band luminosity as 2M1207b and HR8799c and d (Galicher et al. 2014), but has fainter fluxes at shorter wavelengths (this work and De Rosa et al. 2016). Therefore, complementary L' band observations of Sco-Cen targets should be obtained to ensure that planets falling right at the L/T transition are not missed.

6. Constraints on additional giant planets

The observations of HD 95086 with HARPS and SPHERE did not reveal the presence of new planets in the system in addition to HD 95086 b, which is well resolved with both IRDIS and IFS (as described in Sect. 2, see Figs. 1 and 2). The combination of all detection limits can however enable us to constrain the completeness of our study to identify the parameter space in mass and semi-major axis for which planets are detected. After describing below the approaches used to derive the individual detection limits for HARPS and SPHERE, we detail the outcome of a set of Monte-Carlo simulations to probe the probable presence of any additional planets in this young planetary system from a few stellar radii up to 800 au.
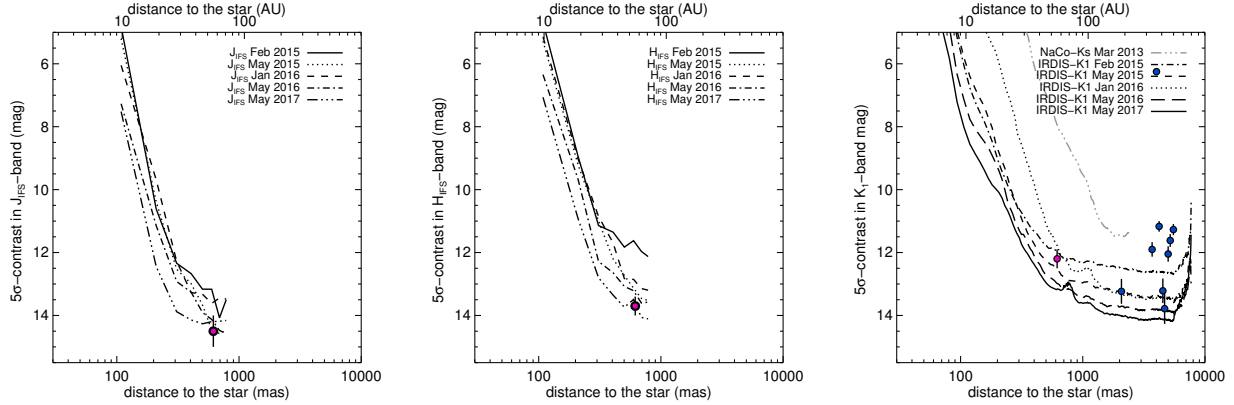
Fig. 12. *Left:* IFS *J*-band detection limit at 5σ based on the spectral PCA analysis using 150 eigen modes obtained in February 3rd, 2015, May 5th, 2015, January 18th, 2016, May 31st, 2016, and May 10th, 2017. Flux loss, coronagraphic transmission and small statistics effects have been corrected. The detection of HD 95086 b combining all epochs is reported in pink with error bars. *Middle*: same as before in *H*-band for the IFS. The planet is also reported in pink with error bars. *Right*: same but for the IRDIS *K*1-band detection limits reported together with all the point-sources detected in the FoV identified as background objects and HD 95086 b reported in pink with error bars.

6.1. Combined HARPS and SPHERE detection limits

For HARPS measurements, we used the local power analysis (LPA) developed by Meunier et al. (2012). This method is based on the generation of periodograms of synthetic planet RV (Radial Velocity) time series, that are compared with the periodogram of the observed RV data within given orbital periods. A detection requires the planet-induced power of the RV signal to be higher than the power of the actual signal within a localized period range. The exploration in mass and period (or semi-major axis) enable to set the detection limit in terms of detection probability. Please refer to Meunier et al. (2012) for a detailed description of the LPA method in comparison with the standard rms or correlation-based approaches (Meunier et al. 2012).

For IRDIS, a standard pixel-to-pixel noise map of each observation was estimated within a box of 5×5 pixels sliding from the star to the limit of the IRDIS and IFS FoV. To correct for the flux loss related to the ADI processing, fake planets were regularly injected every 20 pixels in radius at ten different position angles for separations smaller than 3″. At more than 3″, fake planets were injected every 50 pixels at four different position angles. The final flux loss was computed with the azimuthal average of the flux losses of fake planets at same radii. For IFS, noise maps were also estimated taking account the flux loss with the injection of fake planets, (flat spectra), then summed over the red part between 1.5 and 1.66 μm. The final detection limits at 5σ were then obtained using the pixel-to-pixel noise map divided by the flux loss and normalized by the relative calibration with the primary star (considering the different exposure times, the neutral density and the coronagraph transmission). These detection limits in contrast were finally corrected from small number statistics following the prescription of Mawet et al. (2014) to adapt our 5σ confidence level at small angles with IRDIS and IFS. The results for IRDIS and IFS are reported in Fig. 12.

### 6.2. Planet detection probability around HD 95086

To combine the HARPS and SPHERE detection limits, we used an optimized version of the MESS (multi-purpose exoplanet simulation system) code, a Monte Carlo tool for the statistical analysis and prediction of exoplanet search results (Bonavita et al. 2012). The latest MESS2 version can now handle the combination of radial velocity and direct imaging measurements

obtained at various epochs. Please refer to Lannier et al. (2017) for a detailed description of the code evolution.

In the case of HD 95086, we used MESS2 to generate a uniform grid of mass and semi-major axis in the interval [1, 80] $M_{\rm Jup}$ and [1, 1000] au with a sampling of 0.5 $M_{\rm Jup}$ and 1 au, respectively. The same synthetic planet population is used to explore the detection probability of both HARPS and SPHERE measurements. For each point in the grids, 100 orbits were generated, randomly oriented in space from uniform distributions in cos(i), ω, Ω, $e \leq 0.8$, and T_p. Following the LPA approach described before, the Lomb-Scargle periodograms (Lomb 1976; Scargle 1982) are computed for each generated planet, as well as the periodogram of the observed RV data. Detection probability map are built by counting the number of detected planets over the number of generated ones. The detection threshold is defined when the maximum planet-induced power of the periodogramme is 1.3 times larger than the maximum power of the observed RV data within the period range (Meunier et al. 2012). In addition, the on-sky projected position (separation and position angle) at the time of the observation is computed for each planetary orbit and compared to the SPHERE 5σ 2D-contrast detection maps converted in masses based on the COND model predictions (Baraffe et al. 2003). The primary age, distance, and magnitude (reported in Table 1) are considered for the luminosity-mass conversion. Detection probabilities are built from the number of detected planets over the number of generated ones given our direct-imaging detection threshold.

The MESS2 results merging both HARPS and SPHERE detection probabilities are shown in the left panel of Fig. 13 when no specific orbital constraints are set on the planet properties. Although there is no clear overlap between the radial velocity and direct imaging techniques, the combination of both allows the exploration of giant planets with semi-major axis smaller than 3 au and masses typically larger than 7 $M_{\rm Jup}$ in the best cases and for semi-major axes between typically 15 to 500 au and masses larger than 2 $M_{\rm Jup}$, respectively for detection probability of 90%. For detection probability of 20%, these values decrease to masses larger than 1 $M_{\rm Jup}$ in the best cases for radial velocity at less than 3 au and 2 $M_{\rm Jup}$ between 10 and 1000 au in direct imaging. On the right-panel of Fig. 13 we report the detection probabilities considering planetary orbital solutions that are coplanar with the disk inclination
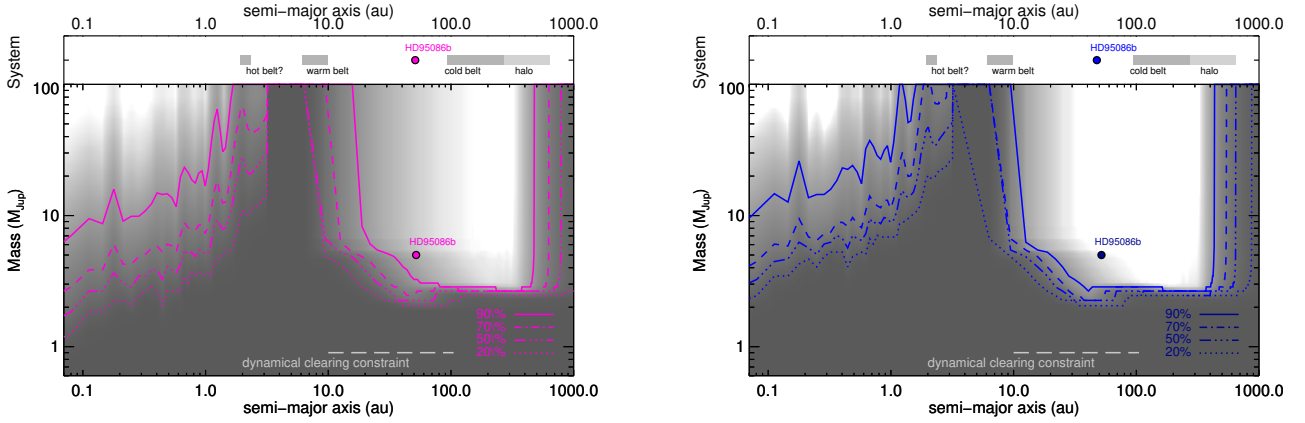
Fig. 13. HARPS and SPHERE combined detection probabilities given as a function of the planet mass and semi-major axis. *Left:* detection probabilities given for planet orbits with no constraints on the inclination, i.e., randomly oriented in space with uniform distributions in $\cos(i)$. Together with HD 95086 b, the dust distribution in the system coming from the combined analysis of the SED fitting and resolved PACS far-IR images is reported with the location of the three components: *warm*, *cold*, *halo* in addition to the possible *hot* one suggested at 2 au. *Right:* detection probabilities with constraints set to restrain solutions to planet orbital inclinations coplanar with the disk inclination of $i = -30 \pm 3°$ and $i = 150 \pm 3°$.

($i = -30 \pm 3°$ and $i = 150 \pm 3°$). These close to face-on solutions logically favor deeper exploration of the close-in physical separations in direct imaging whereas detection probabilities at short periods with radial velocity become less sensitive. In the most optimistic cases, detection probabilities go down to 2 $M_{\rm Jup}$ in radial velocity at less than 3 au and 2 $M_{\rm Jup}$ between 10 and 1000 au in direct imaging for detection probability of 20%. Forthcoming *Gaia* astrometric results on this system will complement the current radial velocity and direct imaging constraints on the population of massive Jovian planets by accessing a typical discovery window between 1 and 10 au.

7. Polarized-light detection of the outer disk

The main properties of the dust distribution studied by Moór et al. (2013), Su et al. (2015) and Su et al. (2017) combining the analysis of the disk SED, PACS far-infrared images and recent ALMA 1.3 mm observations are summarized in Table 6. The detail of the dust temperature and predicted location is given for the four *hot*, *warm*, *cold*, and *halo* components around HD 95086. A key result of the ALMA map is to resolve for the first time the 1.3 mm emission of the *cold* outer belt, which is consistent with a broad ring with sharp boundaries from 106 ± 6 au to 320 ± 20 au.

A prime objective of the IRDIS-DPI observations was to image the disk outer part in *J*-band polarized scattered light at subarcsecond resolution, taking advantage of the spatial resolution achievable with IRDIS (145 mas-diameter for the coronagraphic mask i.e., down to 10 au). The outcome of the DPI data processing of HD 95086, the Q and U Stokes parameters and the Q_ϕ and U_ϕ radial polarized Stokes parameters (see description in Sect. 2.1.1), is reported in Fig. 14. Both Q_ϕ and U_ϕ images were corrected for the disk inclination and position angle, assuming an a-priori knowledge on the disk geometry, and scaled with r^2 to compensate for the r^{-2} dependency on the stellar illumination. No corrections were applied to both Q and U images. Although no obvious signal is detected in the Q_ϕ image compared to U_ϕ, there is a clear Q and U butterfly detection at the location of the *cold* belt and *halo* components fitted by Su et al. (2017; from 106 to 320 au, i.e., 1.2″ to 3.8″). This can be explained by the fact that the oscillating pattern of the Q and U butterfly (which behaves as expected) clearly stands out against the noise, while

Table 6. Disk properties for the hot, warm, cold, and halo components identified in that system based on Su et al. (2015) and updated values of Su et al. (2017).

| Parameter	Unit	*Hot?*	*Warm*	*Cold*	*Halo*
$T_{\rm dust}$	[K]	300	175	55	–
$r_{\rm dust}$	[AU]	~2	7–10	106–320	300–800
Inclination	[°]	–	–	30 ± 3	–
PA	[°]	–	–	97 ± 3	–

Notes. Parameters refer to the temperature of dust ($T_{\rm dust}$), radial location, inclination, and position angle (PA).

for an all positive Q_ϕ or polarized intensity image it is more difficult.

To further explore the presence of a spatially resolved and faint signal in the Q_ϕ image, we calculated the azimuthal average as a function of the radial extent together with the related uncertainties quadratically normalized by the number of elements in each azimuthal ring. The result is reported in Fig. 15. A faint diluted signal emerges from a projected radius of 1.2″ up to 3.5″ (cutoff of sensitivity in our IRDIS DPI observations). It corresponds to deprojected physical separations of 100 and 300 au, respectively. Both pipelines independently confirm the observed over-intensity in Q_ϕ compared to U_ϕ. Although faint, this detection enables for the first time to resolve the polarized scattered light from the cold outer component (and possibly the extended halo) surrounding HD 95086. The detection shows a drop of polarized flux below 1.2″ (~100 au) compatible with the presence of a large cavity between typically 10 and 100 au resulting from the multi-belts analysis combining disk SED, PACS and ALMA images. It also fits with the presence of the closer-in HD 95086 b exoplanet at a semi-major axis of roughly 52 au. Finally, our result corroborates the radial extent of the cold outer belt lying between 100 au up to at least 300 au as observed with ALMA.

8. Planets and belts

The young planetary system around HD 95086 offers an interesting comparison case with HR 8799 (Götberg et al. 2016; Booth
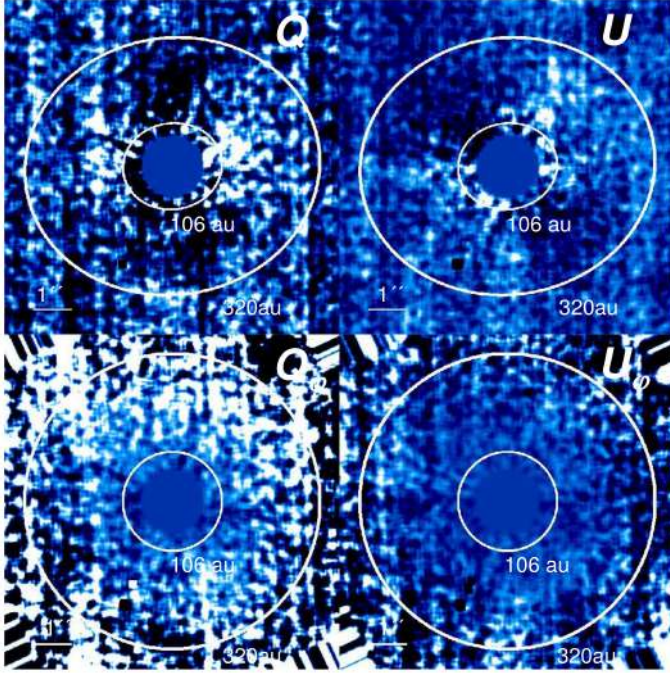
Fig. 14. *Upper-left:* IRDIS *J*-band image of the *Q* Stokes parameter. *Upper-right:* same for the *U* Stokes parameter. North is up and east is toward the left. The location of the inner (106 au) and outer (320 au) edges of the *cold* outer component is superimposed in each case. *Bottom-left:* IRDIS *J*-band image of the Q_ϕ radial polarized Stokes parameter. *Bottom-right:* same for the U_ϕ radial polarized Stokes parameter. Both images were corrected for the disk inclination and position angle and scaled with r^2 to compensate for the r^{-2} dependency on the stellar illumination. Deprojected location of the inner and outer radii of the *cold* outer component is indicated.
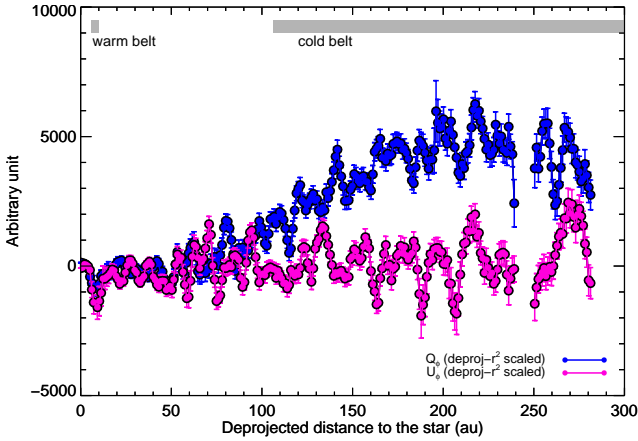
Fig. 15. Azimuthal average of the Q_ϕ, U_ϕ radial polarized Stokes parameters calculated with error bars. Both parameters were corrected for the disk inclination and position angle and scaled with r^2 to compensate for the r^{-2} dependency on the stellar illumination. The location of the warm inner, cold outer, and halo components are indicated.

et al. 2016; Konopacky et al. 2016; Su et al. 2015), and more generally with the interpretation that these multiple-belt debris disks are actually young analogs of our solar system. The presence of planets would be responsible for the dynamical clearing of the debris disk and the formation of observed multi-belt architecture as suggested by Kennedy & Wyatt (2014) and Shannon et al. (2016). In the specific case of HD 95086, one could actually wonder if the presence of additional planets to HD 95086 b would
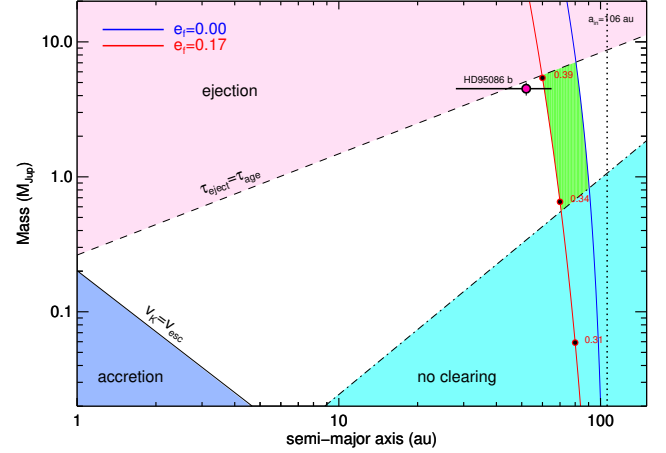
Fig. 16. Constraints on the mass, semi-major axis and eccentricity of the planetary perturber to explain both the inner belt replenishment and the formation and eccentricity upper limit of the outer belt. Light purple and dark blue areas show excluded regions where particles encountering a planetary perturber of given semi-major axis and mass will not remain in the system to replenish the inner belt without being ejected or accreted for timescales younger than the age of the system, respectively. Planets with escape velocity, V_{esc}, larger than the Keplerian velocity, V_K, will most likely eject particles after multiple kicks. On the other hand, if $V_{esc} \ll V_K$ then accretion will likely be the final outcome. This sets the limit shown by the solid black line. In addition, ejection might only happen after several encounters, thus, material can remain in the system for timescales shorter than the ejection timescale. Considering the age of HD 95086, this set the ejection limit shown with the (dashed black line). Moreover, light blue area shows region where the planetary perturber will be not massive enough to stir the disk and carve the outer belt. The blue and red curves delimit dynamical solutions for which the planetary perturber can create an outer belt eccentricity ranging between 0.00 (circular belt) and 0.17 (ALMA upper limit from Su et al. 2017), respectively. Corresponding planetary perturber eccentricities required to create an outer belt eccentricity of 0.17 are overplotted in red. The green area shows the final region for which the planetary perturber semi-major axis, mass and eccentricity meet all the above dynamical constraints to explain both the inner belt replenishment and the formation and eccentricity upper limit of the outer belt. Finally, the predicted location of HD 95086 b by our MCMC orbital fitting analysis is reported in pink with error bars.

be necessary to explain the observed planet – belt architecture including: (i) a warm and relatively narrow inner belt at ~8 au, (ii) a broad cavity from typically 10 to 100 au inside which orbits the massive (4–5 M_{Jup}, $a \sim 52^{+12.8}_{-24.3}$ au and $e = 0.2^{+0.3}_{-0.2}$) planet HD 95086 b, (iii) finally, a cold outer belt lying between 106 and 320 au extending within a disk halo component up to 800 au.

Given that dust has a short lifetime against collisions and radiative forces, the population of small grains in the warm inner belt observed in the spectral energy distribution of HD 95086 must be continuously replenished. Su et al. (2015) rejected P-R drag as a dominant mechanism to transport dust from the outer belt toward the star. They found a maximum amount of material dragged one order of magnitude below what is observed in fractional luminosity for the warm inner belt. An alternative mechanism proposed by Bonsor et al. (2012) to sustain exozodiacal dust originates from small bodies of an outer belt, scattered inward by planets. Their N-body simulations show that a chain of closely spaced, Saturn to Jupiter-mass planets orbiting interior to a massive outer planetesimal belt could replenish exozodiacal dust and sustain an asteroid belt analog.

Marino et al. (2017) applied this scenario to the emblematic case of the 1–2 Gyr old star η Corvi (F2V, 18.3 pc) surrounded

by a hot dust component located at ~1.4 au and a colder one at ~150 au. Considerations of the planet and disk eccentricities, clearing timescale of the chaotic zone as a function of the planet mass and semi-major axis, and the migrating particle escape velocity when encountering the perturbing planet led them to constrain the most probable mass, semi-major axis and eccentricity for the perturbing planet. We applied the same formalism (Eqs. (15)–(19) of Marino et al. 2017) to the younger case of HD 95086 (1.6 $M_\star$, 17 ± 2 Myr) surrounded by an outer belt located at 200 au with an inner boundary at 106 au. We considered in addition an upper limit for the outer belt eccentricity of $e < 0.17$ coming from the nondetection of an outer belt offset in the ALMA 1.3 mm resolved observations of Su et al. (2017). The results are shown in Fig. 16.

The light purple and dark blue areas show excluded regions where particles encountering a planetary perturber will not remain in the system to replenish the inner belt without being ejected or accreted for timescales younger than the age of the system, respectively. The light blue area shows region where the planetary perturber would not be massive enough to stir the disk and carve the outer belt. The resulting white area therefore defines the parameter space for which the planetary perturber will be able to carve the outer belt and replenish the inner belt.

If we add in addition constraints from the outer belt eccentricity obtained by ALMA, the blue and red curves delimit dynamical solutions for which the planetary perturber can create an outer belt eccentricity ranging between 0.00 (circular belt) and 0.17 (ALMA upper limit from Su et al. 2017), respectively. The discrete planetary perturber eccentricities required to create an outer belt eccentricity of 0.17 are indicated in red. The green area shows the final region for the planetary perturber semi-major axis, mass and excentricity where all above dynamical constraints are met to explain both the inner belt replenishment and the formation and eccentricity upper limit of the outer belt.

If we report the orbital properties of HD 95086 b ($a = 52^{+12.8}_{-24.3}$ au and $e = 0.2^{+0.3}_{-0.2}$) and its predicted mass (4–5 $M_{\rm Jup}$), we see that HD 95086 b falls at a location consistent with the predicted properties of the dynamical perturber sculpting the inner boundary of the cold outer component, but for moderate-eccentricity ($e = 0.3$–0.4) solutions. If further astrometric monitoring indicate instead low-eccentricity solutions for HD 95096 b, an additional outer planet at larger semi-major and with masses below ~2 $M_{\rm Jup}$ (given the current detection limits) will have to be considered to explain the observed architecture as proposed by Su et al. (2017).

The broad cavity observed between 10 and 100 au and the current orbital properties of HD 95086 b constrained by GPI and SPHERE suggest anyway that the presence of additional planets is necessary to clear the cavity. In the case of multiple-belt debris disk, Shannon et al. (2016) explored with N-body simulations the minimum planet mass and the expected number of planets that must be present to produce a broad cavity for a star of a given age. If we apply Eqs. (4) and (5) of Shannon et al. (2016) to the case of HD 95086 (1.6 $M_\star$, 17 ± 2 Myr, cavity from 10 to 100 au), we derive a minimum mass of the planets in the cavity of 0.35 $M_{\rm Jup}$ and a typical number of requested planets of 2.4 (i.e., two to three giant planets depending on their respective separation). If we compare these results to the present outcome of the HARPS and SPHERE combined detection limits (Fig. 13, right, coplanar case), we see that there might still be room for two additional stable planets c and d in the cavity in addition to b with typical masses between 0.35 $M_{\rm Jup}$ (dynamical clearing constraint) and 6 $M_{\rm Jup}$ for semi-major axis between 10 and 30 au or 0.35 $M_{\rm Jup}$ and 5 $M_{\rm Jup}$ beyond 30 au. If we rule out the

presence of additional planets at ~8 au owing to the presence of the warm inner belt, closer-in planets might, of course, exist but with less constraining limits in mass of typically 10 to 20 $M_{\rm Jup}$ if orbiting inside 3 au according to our HARPS sensitivity curves. Further N-body simulations tuned for this system would help to refine these conclusions. Although the combination of HARPS and SPHERE in this specific case clearly illustrates the gain of combining techniques (radial velocity and direct imaging) to probe the presence of close-in and wide orbits giant planets in single systems, we see that the new generation of extremely large telescopes in combination with radial velocity and astrometric surveys will be necessary for a global and full exploration of the giant planet population around systems at distances larger than typically 100 pc.

9. Conclusions

In the course of the HARPS large program targeting young, nearby stars and the SHINE and DISK SPHERE GTO programs, we observed the young, planetary system around HD 95086 to explore its global architecture. Our prime goals were to image the cold or halo outer component of the HD 95086 debris disk resolved by *Herschel* in far-IR and recently ALMA at 1.3 mm, to characterize the physical properties of the known imaged planet HD 95086 b (orbital and atmospheric properties), and finally to search for additional planets, constrain their possible physical properties, and discuss them in the light of the formation and viable dynamical configurations of the multi-belt architecture observed in that system. Here, we summarize the main results:

1. We do not detect any additional planet in the system with either HARPS or SPHERE. The 10 point-like sources detected in the SPHERE/IRDIS FoV of 12.5″ × 12.5″ in addition to HD 95086 b are all identified as background objects.

2. HD 95086 b is well resolved with IRDIS in K1 and K2-bands at four epochs between February 2015 and May 2017. The planet's orbital motion is unambiguously resolved. The results of our MCMC orbital fitting analysis favor retrograde orbital solutions of low- to moderate-eccentricity $e \lesssim 0.5$, with a semi-major axis ~52 au corresponding to orbital periods of ~288 yr and an inclination that peaks at $i = 140.7°$, which are still compatible with a planet-disk coplanar configuration.

3. HD 95086 b is imaged at H-band and for the first time in the J-band using the SPHERE IFS instrument by stacking reduced images taken at various epochs to optimize the speckle cancellation. Its near-infrared spectral energy distribution is well fitted by a few dusty and/or young L7–L9 dwarfs. It shows an extremely red 1–4 μm spectral distribution typical of low-gravity effect in the atmospheres of young exoplanets at the L/T transition.

4. The combination of HARPS and SPHERE detection limits offers the unique possibility of exploring and constraining the physical properties of additional giant planets in HD 95086 at close-in and wide orbits. Although there is no clear overlap between both techniques, we reject in the most optimistic cases (detection probability of 20%) and for a planet-disk coplanar configuration the presence of giant planets with masses larger than 2 $M_{\rm Jup}$ to 10 $M_{\rm Jup}$ at less than 3 au and masses larger than 5 $M_{\rm Jup}$ between 10 and 30 au and larger than 2 $M_{\rm Jup}$ beyond 30 au.

5. Finally, the outer debris belt around HD 95086 is resolved for the first time in polarized scattered light by our IRDIS J-band differential polarimetric imaging. The radial extent

of the detected diffused polarized flux is compatible with the location of the cold component recently resolved by ALMA 1.3 mm observations.

6. These results enable us to discuss the presence of additional planets to HD 95086 b in that system to explain the replenishment of warm inner belt located at ∼8 au, the origin of the broad cavity extending between 10 and 100 au, and the observed properties of the cold outer belt beyond 100 au. They illustrate the rich synergy offered by the combination of various observing techniques to explore the global content of giant planets around young, nearby stars and their ability to shape planetary system architectures.

The young planetary system HD 95086 has undoubtedly become one of these rare, enblematic laboratories for the study of giant planet formation as HR 8799 (Marois et al. 2010; Zurlo et al. 2016; Booth et al. 2016), β Pictoris (Lagrange et al. 2010; Dent et al. 2014; Wang et al. 2016), HR 4796 (Perrin et al. 2015; Milli et al. 2017), HD 61005 (Olofsson et al. 2016; Esposito et al. 2016), Fomalhaut (Kalas et al. 2008; MacGregor et al. 2017), AU Mic (Boccaletti et al. 2015; Wang et al. 2015), or TW Hya (Rapson et al. 2015; van Boekel et al. 2017), and HL Tau (ALMA Partnership et al. 2015) at younger ages. HD 95086 will remain a prime target for the SPHERE and GPI planet imagers and high-resolution spectrographs such as HARPS in the coming decade to further explore the presence of additional planets in the system, soon for JWST from space, and for the versatile instrumentation of extremely large telescopes that will bridge the gaps between the different observing techniques to further explore the diversity of this young solar system analog.

References

Allard, F., Homeier, D., & Freytag, B. 2012, Phil. Trans. R. Soc. London, Ser. A, 370, 2765

Allers, K. N., & Liu, M. C. 2013, ApJ, 772, 79
Allers, K. N., Gallimore, J. F., Liu, M. C., & Dupuy, T. J. 2016, ApJ, 819, 133
ALMA Partnership, Brogan, C. L., Pérez, L. M., et al. 2015, ApJ, 808, L3
Artigau, É., Gagné, J., Faherty, J., et al. 2015, ApJ, 806, 254
Avenhaus, H., Quanz, S. P., Schmid, H. M., et al. 2014, ApJ, 781, 87
Bailey, V., Meshkat, T., Reiter, M., et al. 2014, ApJ, 780, L4
Bannister, N. P., & Jameson, R. F. 2007, MNRAS, 378, L24
Baraffe, I., Chabrier, G., Barman, T. S., Allard, F., & Hauschildt, P. H. 2003, A&A, 402, 701
Bayo, A., Rodrigo, C., Barrado Y Navascués, D., et al. 2008, A&A, 492, 277
Benisty, M., Juhasz, A., Boccaletti, A., et al. 2015, A&A, 578, L6
Best, W. M. J., Liu, M. C., Magnier, E. A., et al. 2015, ApJ, 814, 118
Beust, H., Bonnefoy, M., Maire, A.-L., et al. 2016, A&A, 587, A89
Beuzit, J.-L., Feldt, M., Dohlen, K., et al. 2008, Proc. SPIE, 7014, 701418
Blunt, S., Nielsen, E. L., De Rosa, R. J., et al. 2017, AJ, 153, 229
Boccaletti, A., Abe, L., Baudrand, J., et al. 2008, Proc. SPIE, 7015, 70151B
Boccaletti, A., Thalmann, C., Lagrange, A.-M., et al. 2015, Nature, 526, 230
Bonavita, M., Chauvin, G., Desidera, S., et al. 2012, A&A, 537, A67
Bonnefoy, M., Zurlo, A., Baudino, J. L., et al. 2016, A&A, 587, A58
Bonsor, A., Augereau, J.-C., & Thébault, P. 2012, A&A, 548, A104
Booth, M., Jordán, A., Casassus, S., et al. 2016, MNRAS, 460, L10
Borgniet, S., Lagrange, A.-M., Meunier, N., & Galland, F. 2017, A&A, 599, A57
Burgasser, A. J. 2014, in Astronomical Society of India Conference Series, 11, 7
Canovas, H., Ménard, F., de Boer, J., et al. 2015, A&A, 582, L7
Casewell, S. L., Jameson, R. F., & Burleigh, M. R. 2008, MNRAS, 390, 1517
Chauvin, G., Lagrange, A.-M., Dumas, C., et al. 2004, A&A, 425, L29
Chauvin, G., Lagrange, A.-M., Beust, H., et al. 2012, A&A, 542, A41
Chauvin, G., Desidera, S., Lagrange, A.-M., et al. 2017a, A&A, 605, L9
Chauvin, G., Desidera, S., Lagrange, A.-M., et al. 2017b, in SF2A-2017: Proceedings of the Annual meeting of the French Society of Astronomy and Astrophysics, eds. C. Reylé, P. Di Matteo, et al., 331
Chelli, A. 2000, A&A, 358, L59
Chen, C. H., Pecaut, M., Mamajek, E. E., Su, K. Y. L., & Bitner, M. 2012, ApJ, 756, 133
Claudi, R. U., Turatto, M., Gratton, R. G., et al. 2008, Proc. SPIE, 7014, 70143E
Cruz, K. L., Kirkpatrick, J. D., & Burgasser, A. J. 2009, AJ, 137, 3345
Cushing, M. C., Marley, M. S., Saumon, D., et al. 2008, ApJ, 678, 1372
Cutri, R. M., Skrutskie, M. F., van Dyk, S., et al. 2003, The IRSA 2MASS All-Sky Point Source Catalog
Cutri, R. M., Wright, E. L., Conrow, T., et al. 2012, VizieR Online Data Catalog: II/311
de Boer, J., Salter, G., Benisty, M., et al. 2016, A&A, 595, A114
Dent, W. R. F., Wyatt, M. C., Roberge, A., et al. 2014, Science, 343, 1490
De Rosa, R. J., Patience, J., Ward-Duong, K., et al. 2014, MNRAS, 445, 3694
De Rosa, R. J., Rameau, J., Patience, J., et al. 2016, ApJ, 824, 121
Dohlen, K., Langlois, M., Saisse, M., et al. 2008, Proc. SPIE, 7014, 70143L
Draine, B. T. 2003, ARA&A, 41, 241
Ducourant, C., Teixeira, R., Chauvin, G., et al. 2008, A&A, 477, L1
Esposito, T. M., Fitzgerald, M. P., Graham, J. R., et al. 2016, AJ, 152, 85
Faherty, J. K., Burgasser, A. J., Walter, F. M., et al. 2012, ApJ, 752, 56
Faherty, J. K., Rice, E. L., Cruz, K. L., Mamajek, E. E., & Núñez, A. 2013, AJ, 145, 2
Faherty, J. K., Riedel, A. R., Cruz, K. L., et al. 2016, ApJS, 225, 10
Fedele, D., van den Ancker, M. E., Henning, T., Jayawardhana, R., & Oliveira, J. M. 2010, A&A, 510, A72
Filippazzo, J. C., Rice, E. L., Faherty, J., et al. 2015, ApJ, 810, 158
Ford, E. B. 2005, AJ, 129, 1706
Ford, E. B. 2006, ApJ, 642, 505
Fusco, T., Rousset, G., Sauvage, J.-F., et al. 2006, Opt. Exp., 14, 7515
Gagné, J., Lafrenière, D., Doyon, R., et al. 2014a, ApJ, 792, L17
Gagné, J., Lafrenière, D., Doyon, R., Malo, L., & Artigau, É. 2014b, ApJ, 783, 121
Gagné, J., Faherty, J. K., Cruz, K. L., et al. 2015a, ApJS, 219, 33
Gagné, J., Lafrenière, D., Doyon, R., Malo, L., & Artigau, É. 2015b, ApJ, 798, 73
Gaia Collaboration (Brown, A. G. A., et al.) 2016, A&A, 595, A2
Galicher, R., & Marois, C. 2011, in Second International Conference on Adaptive Optics for Extremely Large Telescopes. Online at: http://ao4elt2.lesia.obspm.fr, P25
Galicher, R., Rameau, J., Bonnefoy, M., et al. 2014, A&A, 565, L4
Galland, F., Lagrange, A.-M., Udry, S., et al. 2005, A&A, 444, L21
Gauza, B., Béjar, V. J. S., Pérez-Garrido, A., et al. 2015, ApJ, 804, 96
Gizis, J. E., Faherty, J. K., Liu, M. C., et al. 2012, AJ, 144, 94
Gizis, J. E., Allers, K. N., Liu, M. C., et al. 2015, ApJ, 799, 203
Götberg, Y., Davies, M. B., Mustill, A. J., Johansen, A., & Church, R. P. 2016, A&A, 592, A147
Greco, J. P., & Brandt, T. D. 2016, ApJ, 833, 134
Haisch, Jr. K. E., Lada, E. A., & Lada, C. J. 2001, ApJ, 553, L153

Haisch, Jr. K. E., Jayawardhana, R., & Alves, J. 2005, ApJ, 627, L57
Hinkley, S., Bowler, B. P., Vigan, A., et al. 2015, ApJ, 805, L10
Hiranaka, K., Cruz, K. L., Douglas, S. T., Marley, M. S., & Baldassare, V. F. 2016, ApJ, 830, 96
Høg, E., Fabricius, C., Makarov, V. V., et al. 2000a, A&A, 357, 367
Høg, E., Fabricius, C., Makarov, V. V., et al. 2000b, A&A, 355, L27
Hugot, E., Ferrari, M., El Hadi, K., et al. 2012, A&A, 538, A139
Kalas, P., Graham, J. R., Chiang, E., et al. 2008, Science, 322, 1345
Kellogg, K., Metchev, S., Geißler, K., et al. 2015, AJ, 150, 182
Kellogg, K., Metchev, S., Gagné, J., & Faherty, J. 2016, ApJ, 821, L15
Kennedy, G. M., & Wyatt, M. C. 2014, MNRAS, 444, 3164
Kirkpatrick, J. D., Cushing, M. C., Gelino, C. R., et al. 2011, ApJS, 197, 19
Knapp, G. R., Leggett, S. K., Fan, X., et al. 2004, AJ, 127, 3553
Konopacky, Q. M., Marois, C., Macintosh, B. A., et al. 2016, AJ, 152, 28
Kral, Q., Matrà, L., Wyatt, M. C., & Kennedy, G. M. 2017, MNRAS, 469, 521
Kuhn, J. R., Potter, D., & Parise, B. 2001, ApJ, 553, L189
Lachapelle, F.-R., Lafrenière, D., Gagné, J., et al. 2015, ApJ, 802, 61
Lagrange, A.-M., Bonnefoy, M., Chauvin, G., et al. 2010, Science, 329, 57
Langlois, M., Vigan, A., Moutou, C., et al. 2013, in Proc. Third AO4ELT Conference, eds. S. Esposito, & L. Fini, 63
Langlois, M., Dohlen, K., Vigan, A., et al. 2014, Proc. SPIE, 9147, 91471R
Lannier, J., Lagrange, A. M., Bonavita, M., et al. 2017, A&A, 603, A54
Lazzoni, C., Desidera, S., Marzari, F., et al. 2018, A&A, 611, A43
Lew, B. W. P., Apai, D., Zhou, Y., et al. 2016, ApJ, 829, L32
Liu, M. C., Magnier, E. A., Deacon, N. R., et al. 2013, ApJ, 777, L20
Liu, M. C., Dupuy, T. J., & Allers, K. N. 2016, ApJ, 833, 96
Lomb, N. R. 1976, Ap&SS, 39, 447
Looper, D. L., Kirkpatrick, J. D., Cutri, R. M., et al. 2008, ApJ, 686, 528
Mace, G. N., Kirkpatrick, J. D., Cushing, M. C., et al. 2013, ApJS, 205, 6
MacGregor, M. A., Matrà, L., Kalas, P., et al. 2017, ApJ, 842, 8
Macintosh, B., Graham, J. R., Barman, T., et al. 2015, Science, 350, 64
Madsen, S., Dravins, D., & Lindegren, L. 2002, A&A, 381, 446
Maire, A.-L., Langlois, M., Dohlen, K., et al. 2016, Proc. SPIE, 9908, 990834
Marino, S., Wyatt, M. C., Panić, O., et al. 2017, MNRAS, 465, 2595
Marocco, F., Day-Jones, A. C., Lucas, P. W., et al. 2014, MNRAS, 439, 372
Marois, C., Macintosh, B., Barman, T., et al. 2008, Science, 322, 1348
Marois, C., Zuckerman, B., Konopacky, Q. M., Macintosh, B., & Barman, T. 2010, Nature, 468, 1080
Marois, C., Correia, C., Véran, J.-P., & Currie, T. 2014, IAU Symp., 299, 48
Marshall, J. P., Moro-Martín, A., Eiroa, C., et al. 2014, A&A, 565, A15
Mawet, D., Milli, J., Wahhaj, Z., et al. 2014, ApJ, 792, 97
McCaughrean, M. J., & Stauffer, J. R. 1994, AJ, 108, 1382
McLean, I. S., McGovern, M. R., Burgasser, A. J., et al. 2003, ApJ, 596, 561
Mesa, D., Gratton, R., Zurlo, A., et al. 2015, A&A, 576, A121
Mesa, D., Vigan, A., D'Orazi, V., et al. 2016, A&A, 593, A119
Meshkat, T., Bailey, V., Rameau, J., et al. 2013, ApJ, 775, L40
Meunier, N., Lagrange, A.-M., & De Bondt, K. 2012, A&A, 545, A87
Milli, J., Vigan, A., Mouillet, D., et al. 2017, A&A, 599, A108
Moór, A., Ábrahám, P., Kóspál, Á., et al. 2013, ApJ, 775, L51
Nilsson, R., Liseau, R., Brandeker, A., et al. 2010, A&A, 518, A40
Olofsson, J., Samland, M., Avenhaus, H., et al. 2016, A&A, 591, A108
Oppenheimer, B. R., Baranec, C., Beichman, C., et al. 2013, ApJ, 768, 24
Patience, J., King, R. R., de Rosa, R. J., & Marois, C. 2010, A&A, 517, A76
Pavlov, A., Möller-Nilsson, O., Feldt, M., et al. 2008, Proc. SPIE, 7019, 701939
Pecaut, M. J., Mamajek, E. E., & Bubar, E. J. 2012, ApJ, 746, 154
Pepe, F., Mayor, M., Rupprecht, G., et al. 2002, The Messenger, 110, 9
Perrin, M. D., Duchene, G., Millar-Blanchaer, M., et al. 2015, ApJ, 799, 182
Petit, C., Sauvage, J.-F., Fusco, T., et al. 2014, Proc. SPIE, 9148, 91480O
Pueyo, L., Soummer, R., Hoffmann, J., et al. 2015, ApJ, 803, 31
Rameau, J., Chauvin, G., Lagrange, A.-M., et al. 2013a, ApJ, 772, L15
Rameau, J., Chauvin, G., Lagrange, A.-M., et al. 2013b, A&A, 553, A60
Rameau, J., Chauvin, G., Lagrange, A.-M., et al. 2013c, ApJ, 779, L26
Rameau, J., Nielsen, E. L., De Rosa, R. J., et al. 2016, ApJ, 822, L29
Rapson, V. A., Kastner, J. H., Millar-Blanchaer, M. A., & Dong, R. 2015, ApJ, 815, L26
Rebolo, R., Zapatero Osorio, M. R., Madruga, S., et al. 1998, Science, 282, 1309
Reid, I. N., Lewitus, E., Allen, P. R., Cruz, K. L., & Burgasser, A. J. 2006, AJ, 132, 891
Rich, E. A., Currie, T., Wisniewski, J. P., et al. 2016, ApJ, 830, 114
Rizzuto, A. C., Ireland, M. J., & Zucker, D. B. 2012, MNRAS, 421, L97
Samland, M., Mollière, P., Bonnefoy, M., et al. 2017, A&A, 603, A57
Sauvage, J.-F., Fusco, T., Petit, C., et al. 2010, Proc. SPIE, 7736, 77360F
Sauvage, J.-F., Fusco, T., Lamb, M., et al. 2016, Proc. SPIE, 9909, 990916
Scargle, J. D. 1982, ApJ, 263, 835
Schmid, H. M., Joos, F., & Tschan, D. 2006, A&A, 452, 657
Schneider, A. C., Cushing, M. C., Kirkpatrick, J. D., et al. 2014a, AJ, 147, 34
Schneider, G., Grady, C. A., Hines, D. C., et al. 2014b, AJ, 148, 59
Scott, A., & Duley, W. W. 1996, ApJS, 105, 401
Shannon, A., Bonsor, A., Kral, Q., & Matthews, E. 2016, MNRAS, 462, L116
Siess, L., Dufour, E., & Forestini, M. 2000, A&A, 358, 593
Soummer, R. 2005, ApJ, 618, L161
Soummer, R., Pueyo, L., & Larkin, J. 2012, ApJ, 755, L28
Stephens, D. C., Leggett, S. K., Cushing, M. C., et al. 2009, ApJ, 702, 154
Stone, J. M., Eisner, J., Skemer, A., et al. 2016a, ApJ, 829, 39
Stone, J. M., Skemer, A. J., Kratter, K. M., et al. 2016b, ApJ, 818, L12
Su, K. Y. L., Morrison, S., Malhotra, R., et al. 2015, ApJ, 799, 146
Su, K. Y. L., Macgregor, M. A., Booth, M., et al. 2017, AJ, 154, 225
Thalmann, C., Schmid, H. M., Boccaletti, A., et al. 2008, Proc. SPIE, 7014, 70143F
van Boekel, R., Henning, T., Menu, J., et al. 2017, ApJ, 837, 132
van Leeuwen, F. 2007, A&A, 474, 653
Viana Almeida, P., Santos, N. C., Melo, C., et al. 2009, A&A, 501, 965
Vigan, A., Moutou, C., Langlois, M., et al. 2010, MNRAS, 407, 71
Wagner, K., Apai, D., Kasper, M., et al. 2016, Science, 353, 673
Wang, J. J., Graham, J. R., Pueyo, L., et al. 2015, ApJ, 811, L19
Wang, J. J., Graham, J. R., Pueyo, L., et al. 2016, AJ, 152, 97
Zurlo, A., Vigan, A., Galicher, R., et al. 2016, A&A, 587, A57

1 Université Grenoble Alpes, CNRS, IPAG, 38000 Grenoble, France
  e-mail: gael.chauvin@univ-grenoble-alpes.fr
2 Unidad Mixta Internacional Franco-Chilena de Astronomía, CNRS/INSU UMI 3386 and Departamento de Astronomía, Universidad de Chile, Casilla 36-D, Santiago, Chile
3 INAF - Osservatorio Astronomico di Padova, Vicolo dell' Osservatorio 5, 35122 Padova, Italy
4 Leiden Observatory, Universiteit Leiden, PO Box 9513, 2300 RA Leiden, The Netherlands
5 Aix-Marseille Université, CNRS, LAM - Laboratoire d'Astrophysique de Marseille, UMR 7326, 13388 Marseille, France
6 LESIA, Observatoire de Paris, PSL Research University, CNRS, Sorbonne Universités, UPMC Univ. Paris 06, Univ. Paris Diderot, Sorbonne Paris Cité, 5 place Jules Janssen, 92195 Meudon, France
7 Max Planck Institute for Astronomy, Königstuhl 17, 69117 Heidelberg, Germany
8 Konkoly Observatory, Research Centre for Astronomy and Earth Sciences, Hungarian Academy of Sciences, PO Box 67, 1525 Budapest, Hungary
9 Institute for Astronomy, ETH Zurich, Wolfgang-Pauli-Strasse 27, 8093 Zurich, Switzerland
10 Department of Astronomy, Stockholm University, AlbaNova University Center, 106 91 Stockholm, Sweden
11 SUPA, Institute for Astronomy, The University of Edinburgh, Royal Observatory, Blackford Hill, Edinburgh EH9 3HJ, UK
12 Geneva Observatory, University of Geneva, Chemin des Mailettes 51, 1290 Versoix, Switzerland
13 Anton Pannekoek Institute for Astronomy, Science Park 904, 1098 XH Amsterdam, The Netherlands
14 Université Côte d'Azur, OCA, CNRS, Lagrange, France
15 CRAL, UMR 5574, CNRS, Université de Lyon, École Normale Supérieure de Lyon, 46 Allée d'Italie, 69364 Lyon Cedex 07, France
16 INAF-Catania Astrophysical Observatory, via S. Sofia 78, 95123 Catania, Italy
17 Núcleo Milenio Formación Planetaria - NPF, Universidad de Valparaíso, Av. Gran Bretaña 1111, Valparaíso, Chile
18 Núcleo de Astronomía, Facultad de Ingeniería y Ciencias, Universidad Diego Portales, Av. Ejercito 441, Santiago, Chile
19 Escuela de Ingeniería Industrial, Facultad de Ingeniería y Ciencias, Universidad Diego Portales, Av. Ejercito 441, Santiago, Chile
20 INCT, Universidad De Atacama, calle Copayapu 485, Copiapó, Atacama, Chile

Appendix A: Conversion to flux

We gathered the optical to mid-IR photometry of the star HD 95086 using VOSA[4] (Bayo et al. 2008). The measurements were then adjusted by a BT-NEXTGEN synthetic spectrum to derive the physical fluxes of HD 95086 and HD 95086 b in each filter and spectral channel used for the characterization of the spectral energy distribution of HD 95086 b.
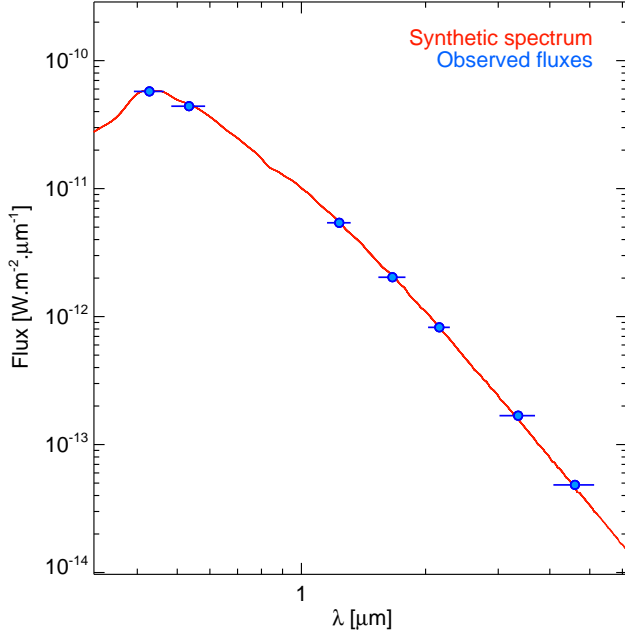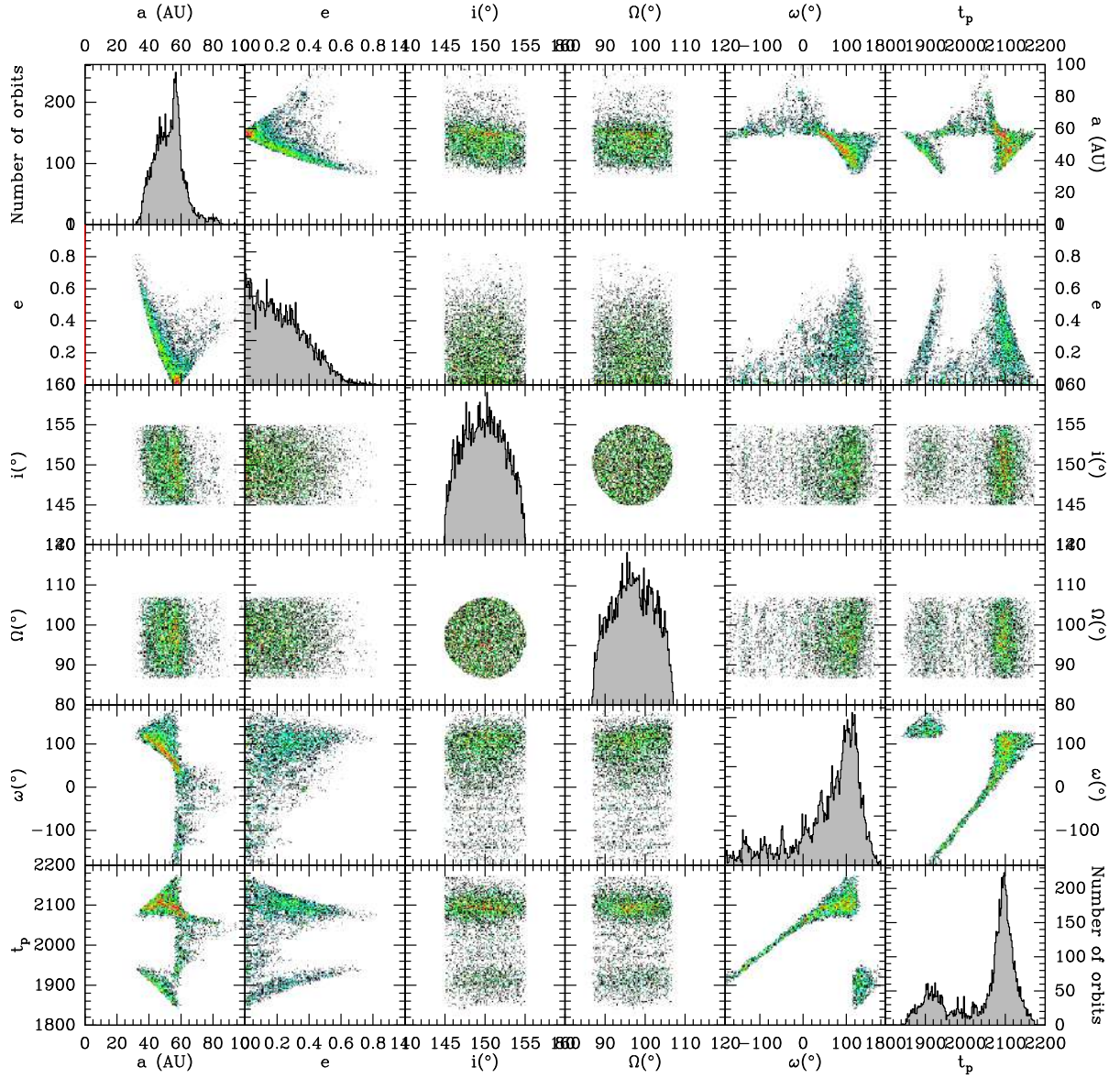

Fig. A.1. BT-NEXTGEN synthetic spectrum (red curve) adjusted onto the star HD 95086 photometry (blue dots).

Appendix B: Markov-chain Monte-Carlo inclination-restricted results

Fig. B.1. Results of the MCMC fit of the NaCo and SPHERE combined astrometric data of HD 95086 b reported in terms of statistical distribution matrix of the orbital elements a, e, i, Ω, ω and t_p. The red line indicates the position of the best LSLM χ^2_r model obtained for comparison. The reported solutions correspond for the restricted case of orbits with inclination i and longitudes of ascending nodes Ω that ensure a tilt angle with the outer belt resolved with *ALMA* ($i = 150°$, $\Omega = 97°$, Su et al. 2017) less than 5°.

Appendix C: Markov-chain Monte-Carlo results for combined NaCo and GPI measurements
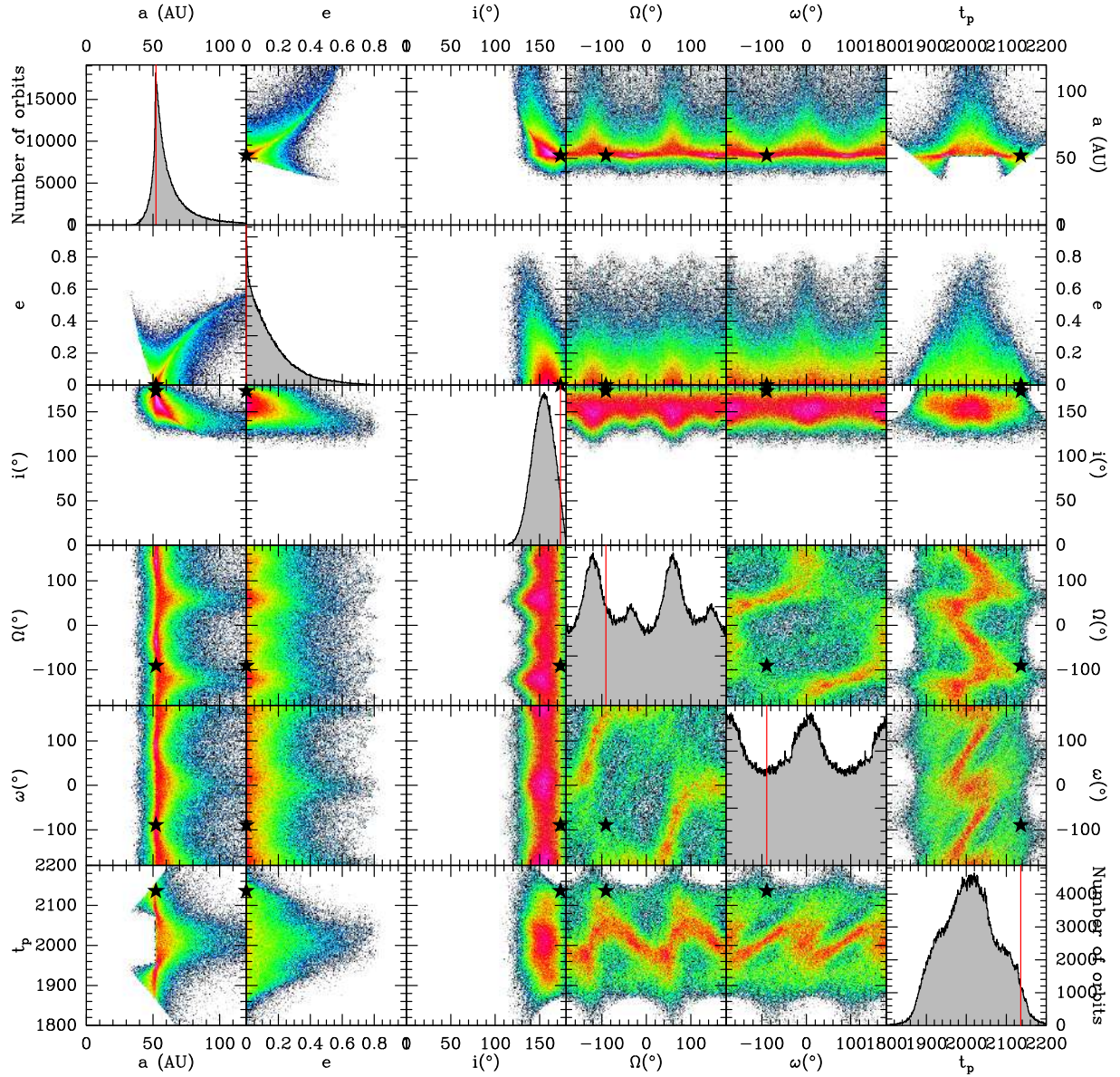
Fig. C.1. Results of the MCMC fit of the NaCo and GPI combined astrometric data of HD 95086 b. Measurements are directly taken from Table 1 of Rameau et al. (2016). The results are reported in terms of statistical distribution matrix of the orbital elements a, e, i, Ω, ω and t_p. The red line indicates the position of the best LSLM χ_r^2 model obtained for comparison. Considering the new distance estimate of 83.8 pc, a correction factor of 0.93 in sma and 0.89 in period must be applied for direct comparison with Fig. 3 of Rameau et al. (2016). The MCMC tool used in this work and the MCMC OFTI tool of Blunt et al. (2017) show a relatively good match confirming both MCMC methods.

Appendix D: Benchmark dusty L dwarfs

Table D.1. Properties of dusty, peculiar, and possibly young, dwarfs later than L4 considered in our study.

Source name	Spectral type	Membership	Mass ($M_{\rm Jup}$)	Reference
2MASS J11193254-1137466	L7	TWA	4.3–7.6	1, 2
2MASS J17081563+2557474	L5	. . .	. . .	1
WISEP J004701.06+680352.1	L7	AB Dor	~18	3, 4
PSO J318.5338-22.8603	L7	β Pic	8.3 ± 0.5	5, 6
ULAS J222711-004547	L7	. . .	. . .	7
WISE J174102.78-464225.5	L7	β Pic or AB Dor	4–21	8
WISE J020625.27+264023.6	L8	. . .	. . .	9, 22
WISE J164715.57+563208.3	L9	Argus	4-5	9, 10
2MASS J00011217+1535355	L4	AB Dor	25.3 ± 1.0	11, 12, 13
2MASS J21543454-1055308	L4	Argus?	. . .	14, 22
2MASS J22064498-4217208	L4	AB Dor	23.1 ± 6.4	15
2MASS J23433470-3646021	L3–L6	AB Dor	. . .	12
2MASS J03552337+113343	L5	AB Dor	13–30	16, 17, 18
2MASS J21481628+4003593	L6	Argus?	. . .	10, 15, 19, 22
2MASSW J2244316+204343	L6	AB Dor	11–12	15, 20
2MASSJ05012406–0010452	L4	Columba	$10.2^{+0.8}_{-1.0}$	12, 21

References. 1 – Kellogg et al. (2015), 2 – Kellogg et al. (2016), 3 – Gizis et al. (2012), 4 – Gizis et al. (2015), 5 – Liu et al. (2013), 6 – Allers et al. (2016), 7 – Marocco et al. (2014), 8 – Schneider et al. (2014a), 9 – Kirkpatrick et al. (2011), 10 – Gagné et al. (2014b), 11 – Knapp et al. (2004), 12 – Gagné et al. (2015a), 13 – Gagné et al. (2015b), 14 – Gagné et al. (2014a), 15 – Faherty et al. (2016), 16 – Reid et al. (2006), 17 – Cruz et al. (2009), 18 – Faherty et al. (2013), 19 – Looper et al. (2008), 20 – McLean et al. (2003), 21 – Casewell et al. (2008), 22 – Liu et al. (2016).